

## The Feasibility of Neutron Moderation Imaging for Land Mine Detection

**John E. McFee\*** and Anthony Faust

Defence R&D Canada—Suffield, Box 4000, Station Main, Medicine Hat, AB, Canada T1A 8K6

**H. Robert Andrews, Ted Clifford, and Harry Ing**

Bubble Technology Industries, Highway 17, Box 100, Chalk River, ON, Canada K0J 1J0

**Tom Cousins and Dean Haslip**

Defence R&D Canada—Ottawa, 3701 Carling Ave., Ottawa, ON, Canada K1A 0K2

*Received July 10, 2001; revised August 8, 2002*

---

Neutron moderation land mine detection involves irradiating the ground with fast neutrons and subsequently detecting the thermalized neutrons which return. This technique has been studied since the 1950s, but only using non-imaging detectors. Without imaging, natural variations in moisture content, surface irregularities, and sensor height variations produce sufficient false alarms to render the method impractical in all but the driest conditions. This paper describes research to design and build a prototype land mine detector based on neutron moderation imaging. After reviewing various neutron detector technologies, a design concept was developed. It consists of a novel thermal neutron imaging system, a unique neutron source to uniformly irradiate the underlying ground, and hardware and software for image generation and enhancement. A proof-of-principle imager has been built, but with a point source offset from the detector to roughly approximate a very weak uniform source at the detector plane. Imagery from the detector of mine surrogates is presented. Realistic Monte Carlo simulations were performed using the same two dimensional neutron imaging geometry as the detector in order to assess its performance. **The target-to-background contrast was calculated for various**

---

\*To whom all correspondence should be addressed. Telephone: 403-544-4739; fax: 403-544-4704; e-mail: John.McFee@drdc-rddc.gc.ca

soil types and moisture contents, explosive types and sizes, burial depths, detector standoffs, and ground height variations. The simulations showed that the neutron moderation imager is feasible as a land mine detector **in a slow scanning or confirmation role** and that image quality should be sufficient to significantly improve detector performance and reduce false alarm rates compared to non-imaging albedo detection, particularly in moist soils, where surface irregularities exist and when the sensor height is uncertain. Performance capability, including spatial resolution and detection times, was estimated.

---

**Key Words:** Neutron moderation imaging, neutron albedo imaging, land mine detection.

## 1. Introduction

Detection of land mines using nuclear techniques has been studied exhaustively since the 1950s. Virtually every conceivable nuclear reaction has been examined, but after considering such factors as penetration, sensitivity, selectivity, size, weight, and power, only a very few have potential for land mine detection [1,2,3,4]. Lateral migration X-ray backscatter imaging [5] and thermal neutron activation (TNA) are among the most promising for vehicle mounted applications and are still being actively investigated. The only known nuclear-based land mine detector that is commercially available is a production version of a Californium-based thermal neutron activation detector [6,7] developed as a confirmation sensor for the Canadian Improved Landmine Detection System (ILDS), a vehicle-mounted, multisensor, land mine detector system [8]. A prototype neutron generator-based version is now undergoing testing [9]. The latter systems are restricted to detecting antitank (AT) and large antipersonnel (AP) land mines. The number of nuclear reactions having potential for adaptation to handheld, antipersonnel land mine detection is even smaller. These typically involve the use of larger cross sections and more efficient detectors which allow relatively weak sources to be used. This allows a decrease in size and weight of shielding for electronics and personnel. Among them are uncollimated X-ray backscatter imaging [10] and neutron moderation imaging. The latter is the subject of this paper.

There are few candidate confirmation detectors for AP mines. Uncollimated X-ray backscatter imaging detectors for land mine detection are still at the simulation stage. A prototype electrical impedance tomography detector has produced low spatial resolution mine images in several seconds [11] in some soil types. However, it requires probes to be pushed into the ground over the mine, making it potentially hazardous to use. Nuclear quadrupole resonance, a radiofrequency resonant absorption technique, can in principle give a signal that is characteristic of the explosive filling. It has demonstrated its ability to detect RDX-filled mines in field trials [12]. Detection of TNT-filled mines, which constitute >90% of all land mines, is

much more difficult, since the signal-to-noise ratio is an order of magnitude smaller. Other things, such as the piezoelectric effect from quartz bearing soil, magnetic soil, temperature dependence of resonant frequency, and depth dependence of response, affect the signal quality and ability to detect. By far the biggest problem is radiofrequency interference, since the signals are minuscule and the resonant frequencies occur in the AM radio waveband for TNT. Presently, RF noise can only be reduced by recording noise in a base station and applying compensation algorithms off line. Even then, TNT-filled AP mines are not reliably detected. It will be seen that neutron moderation has none of these problems. Its chief source of interference is ground water.

Neutron moderation or thermalization without imaging has been studied for land mine detection in some detail [1,3]. Explosives contain 2–3% hydrogen by weight, while soils may contain from 0% to over 50% hydrogen [4]. Thus the presence of an anomaly in the measurement of hydrogen density may be used to imply the presence of a land mine. The method involves irradiating an area with fast neutrons and detecting the subsequently moderated and returned slow neutrons. Measurement of the albedo (ratio of number of slow neutrons returned from the soil to the number of incident fast neutrons) is then used as an indicator of the presence of a mine. The chief limiting factor in the target-to-clutter ratio is hydrogen in ground water. The hydrogen densities of the soil and the land mine will be equal when the gravimetric percentage of water is between 18 and 27%, and hence mines cannot be detected in this range. In practice, moisture contents in excess of 10% have rendered this detection technique ineffective in the past. Other factors which can limit the target-to-clutter ratio are ground surface irregularities and detector height variations.

Research in neutron moderation detection of land mines has been conducted since the early 1950s and has continued through to the 1990s, mainly for the US Army. Isotopic sources, such as Po–Be and Cf, with typical outputs of  $10^6$  n/s, have been used. Accelerator sources have employed different reactions to yield neutron energies of 1.1, 2.8, and 14.8 MeV. Detectors have included  $\text{BF}_3$  and  $^3\text{He}$  proportional counters and  $^6\text{LiI}$  crystals wrapped in Cd.  $\text{BF}_3$  or  $^3\text{He}$  multiwire proportional counters for imaging have been proposed [1], but were never employed in this role.

At a workshop in 1985 to identify nuclear techniques suitable for land mine detection [3], experts placed neutron moderation among the top three techniques, after X-ray backscatter imaging and thermal neutron capture gamma rays (TNA). In spite of this, neutron moderation has not been very successful to date, while TNA is now a fielded confirmation detection technology for a vehicle-mounted system [6,7,8]. The reason for this is that natural variations in hydrogen content in the soil, chiefly due to water, and

surface irregularities and detector height variations all effect the albedo contrast. This produces enough false alarms to make the neutron moderation method impractical in all but the driest conditions. For instance, at the invitation of the US government, DRDC Suffield scientists participated in testing of a neutron moderation detector, built by SAIC US, at 29 Palms, CA in December, 1993. The system, which consisted of four  $^3\text{He}$  detectors and a weak ( $\sim 10^6$  n/s)  $^{252}\text{Cf}$  source, produced an unacceptably high false alarm rate, even though the environment was a flat, clean section of dry desert. Nevertheless, there are a few groups currently involved in research on neutron moderation detection of land mines. Frank Brooks, University of Capetown [13] and Carel W.E. van Eijk, Delft University [14], both have programs of simulation and experimentation. Richard Craig, Pacific Northwest National Laboratory, has been investigating the use of a time-tagged neutron source to help discriminate between soil and explosives. All three groups have focused on nonimaging detection.

One method of reducing false alarms is to spatially image the neutrons coming from the ground. Although this has been proposed previously [1], to date it does not appear to have been tried. This paper describes research to determine the feasibility and practicality of designing and building a land mine detector based on neutron moderation imaging. A design concept for the imager will be presented. It consists of a novel thermal neutron imaging system, a unique neutron source to uniformly irradiate the underlying ground and hardware and software for image generation and enhancement. A proof-of-principle imager has been built, but with a point source offset from the detector to roughly approximate the weak uniform source at the detector plane that will ultimately be used. Preliminary imagery from the detector of land mine surrogates will be presented.

Realistic Monte Carlo simulations were performed using the same two dimensional neutron imaging geometry as the detector in order to assess its performance. The target-to-background contrast was calculated for various relevant parameters, such as soil type and moisture content, explosive type and mass, mine burial depth, detector standoff and ground height variations due to surface roughness. Performance capability, including spatial resolution and detection times, was estimated from the model. The simulations and their results will be described.

The simulations and images show that the neutron moderation imager is feasible as a land mine detector in a slow scanning or confirmation role and that image quality should be sufficient to significantly improve detector performance and reduce false alarm rates compared to non-imaging albedo detection, particularly in moist soils, where surface irregularities exist and when the sensor height is uncertain.

## 2. Instrument Design

A variety of neutron detector technologies were reviewed, taking into account the requirement for adequate spatial imaging resolution, ease of use, minimum weight and acceptable system cost. The most appropriate technology for the application was selected to form the basis of the conceptual design which is described in this section.

A photograph of the detection unit for the prototype instrument is shown in Figure 1. The detector/source assembly is a 50 cm  $\times$  50 cm light-tight housing containing a planar neutron scintillation imager and a coplanar neutron source. The imager is coupled via a fiber optics bundle to a photomultiplier and processing electronics situated in a box attached to the top of the detector/source assembly. Instrument mass is roughly 13 kg and power consumption is about 10 W, supplied by batteries.

In addition to the detection unit there is a remote analysis unit (computer) connected by a wireless or hardwired serial link. This separation of

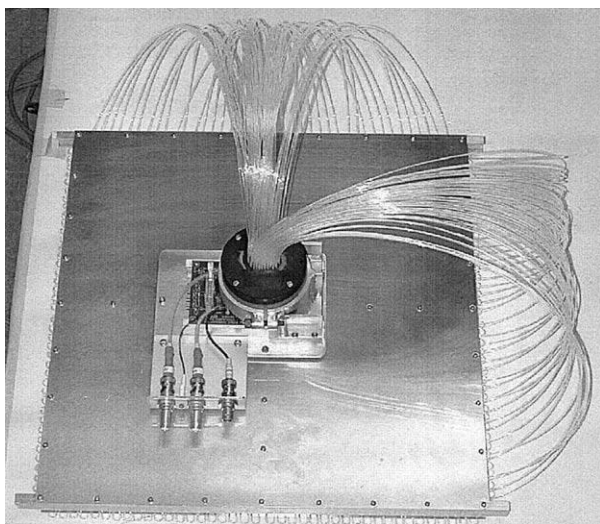


**Figure 1.** Photograph of the top of the neutron moderation imager detection unit, removed from its light-tight shield. It consists of a neutron-sensitive scintillation screen sandwiched between a crossed ( $X, Y$ ) grid of position-sensing, wavelength shifting optical fibers and a uniform sheet Californium source. Each optical fiber wraps back and forth parallel to itself in the image plane to increase its effective path length. This can be seen as a series of  $U$ s along the edges of the detector. The ends of the fibers can be seen exiting from the detector plane and entering the multi-dynode photomultiplier tube which is used to decode neutron position. A detailed description is given in Section 2.

function is intended to minimize radiation exposure to the operator from the albeit weak neutron source resident in the detection unit.

The two key components of the instrument are the thermal neutron imager and a unique neutron source to uniformly irradiate the underlying ground. These are discussed more fully in the next two subsections.

## 2.1. Thermal Neutron Imager

A schematic diagram of a small portion ( $\sim 2\text{ cm} \times \sim 2\text{ cm}$ ) of the detection unit is shown in Figure 2 and a block diagram of the instrument electronics is shown in Figure 3. The imaging approach chosen was to use a scintillation screen coupled to arrays of orthogonally crossed ( $X, Y$ ) wavelength shifting optical fibers. A similar approach has been tried previously using wavelength shifting optical fibers or wavelength shifter bars for small area ( $<1\text{ cm} \times 1\text{ cm}$ ) neutron detection [15] and for areas as large as  $25\text{ cm} \times 25\text{ cm}$  [16]. The scintillator must detect thermal neutrons and reject fast neutrons. A ZnS:Ag scintillation screen with  ${}^6\text{LiF}$  dispersed through it, was chosen as the detection medium. The  ${}^6\text{Li}(n,\alpha){}^3\text{H}$  reaction has a high

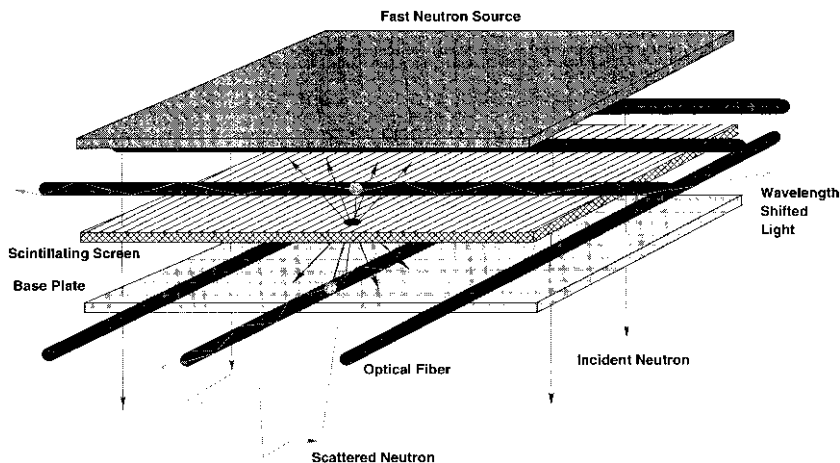


**Figure 2.** Schematic of a small portion ( $\sim 2\text{ cm} \times 2\text{ cm}$ ) of the neutron moderation imager detection unit. It consists of a neutron-sensitive scintillation screen sandwiched between a crossed grid of wavelength shifting fibers and a uniform sheet Californium neutron source. Coincident light signals (two light dots), corresponding to scintillation from a detected neutron event (dark dot), travel along an  $X, Y$  pair of fibers to a multi-dynode photomultiplier tube. Auxiliary electronics decode the neutron position. For clarity each fiber is shown making a single pass over the screen, but in the actual imager each fiber passes back and forth parallel to itself four times. A detailed description is given in Section 2.

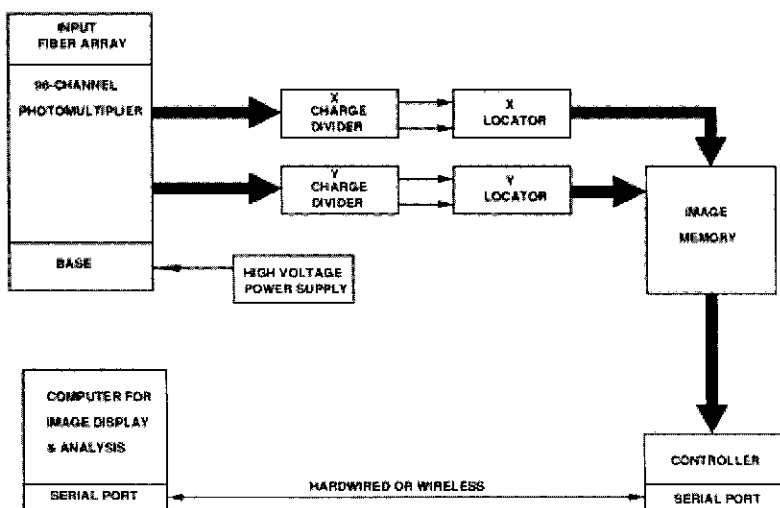


**Figure 3.** Block diagram of the neutron albedo imager electronics. A neutron produces a pulse in specific  $X$  and  $Y$  fibers. Charge division analysis of the corresponding photomultiplier dynode outputs is used to decode the correct  $X$  and  $Y$  fibers. The corresponding position in image memory is then incremented. A detailed description is given in Section 2.

cross section for thermal neutrons and a high positive  $Q$  value (4.78 MeV) which is converted into the kinetic energy of the  $\alpha$  and triton. The energetic charged particles produce scintillations in the ZnS:Ag.  $^6\text{Li}$  glass scintillators have been used with wavelength shifter bars and optical fibers to image thermal neutrons over small areas [17]. They were considered, but the materials costs were prohibitively expensive for the large area required.

The active area of the detector is  $40\text{ cm} \times 40\text{ cm}$  with  $1\text{ cm} \times 1\text{ cm}$  pixels. The detector area was chosen to allow the largest common AT mines ( $\sim 30\text{ cm}$  diameter) to be covered with a reasonable buffer space on each side to allow background estimation. Although it would be desirable to make the area larger to include more background, this would make the instrument impractical for handheld use. The  $1\text{ cm}$  pixels were chosen to assure a reasonably large number of pixels (at least 25 full pixels) across the smallest buried AP mines (typically  $\sim 6.5\text{ cm}$  diameter) while minimizing instrument complexity. Further, as will be seen, backscattered neutron distributions are reasonably smooth on a  $1\text{--}2\text{ cm}$  resolution scale. The scintillator screen is deposited on a glass substrate and is positioned between the  $X$  and  $Y$  arrays of fibers. Above the upper fiber array is a boron layer (not shown in Figure 2) to absorb thermal neutrons from the source. The top layer is the planar source with the same dimensions as the active detector.

The neutron detection medium is an Applied Scintillation Technologies  ${}^6\text{LiF}/\text{ZnS}:\text{Ag}$  neutron radiography screen. It emits radiation in the blue, peaking at 450 nm. The 1 mm diameter wavelength shifting fibers are Bicon BCF-91A, which absorb below 450 nm and emit around 500 nm. Each of the 80 (40X and 40Y) fibers passes back and forth, parallel to itself, four times over the screen to increase the effective path length. (For clarity in Figure 2, each fiber is shown making only one pass.) Both ends of each fiber are glued into a precision-machined faceplate, which positions them over the appropriate pixel of the photocathode of a Philips XP1724 96-channel multi-dynode photomultiplier tube (PMT). In practice the bends in the fiber extend somewhat beyond the detector body to increase their radii so as to maximize light transmission to the fiber ends.

Roughly  $1.7 \times 10^5$  photons are emitted in the scintillator screen per thermal neutron event. The number of photons per event reaching the PMT photocathode can be estimated as follows. Approximately one half of the photons exit each side of the screen. The absorption length in the wavelength shifter is about 5 mm and the effective thickness of the fiber array (assumed distributed as a 1 cm-wide bar) is 0.314 mm. Thus, the fraction of light shifted on a single pass is 0.061. This must be reduced by a factor of 2 because only about half of the blue light is of short enough wavelengths to be shifted. The fraction of the shifted light captured and transmitted by the fiber is  $\sim 0.034$  and it is assumed that transmission loss due to the fairly tight bends in the fiber is about 0.5. Combining these factors, the predicted number of X and Y photons reaching the PMT photocathode is about 45 each per event. The PMT is operated in single-photon-counting mode, so that good coincidence efficiency is possible.

Light pulses from the X and Y optical fibers are processed by the system electronics (Fig. 3), which consists of the detector, the fiber-optic links to the multichannel PMT, the X and Y charge dividers, the X and Y locators, image memory and a controller which handles command and control and transmission of data to the analysis station.

The PMT has a 96 segment tenth dynode (of which 80 are used), with each segment corresponding to a pixel on the photocathode. The X and Y wavelength-shifter fibers are optically coupled to the photocathode so that each time a fiber is excited, an electronic pulse appears on the corresponding dynode segment. Each neutron event in the detector will excite one unique combination of X and Y fibers, which gives the coordinates of the location of the event.

Charge division is used to identify the pair of dynode segments that have signals. This eliminates the need for 80 amplifiers and discriminators. There are two groups of shifter fibers and hence dynode segments; one for

the  $X$  coordinates and one for the  $Y$  coordinates. For each group, the segments are connected to a chain of 40 resistors (assuming a  $40 \times 40$  array of fibers). Each end of the chain leads to a charge-sensitive amplifier. Because the ratio of charge reaching the amplifiers depends on the position of the corresponding dynode on the resistive chain, the ratios of amplifier output signals uniquely identifies the  $X$  and  $Y$  segments (and hence detector coordinate) responsible for the event.

The data-processing electronics are designed to minimize the time required to process events. To this end, analog dividers and fast analog to digital converters (ADCs) are used to process the  $X$  and  $Y$  coordinate data in the charge dividers. In the locators, field-programmable-gate arrays (FPGAs) are used to sort the ADC outputs into  $X$  and  $Y$  coordinate bins in the image memory. The operation is supervised by a microprocessor, which looks after packaging the image data, transmitting it periodically to the analysis computer, and receiving commands from the latter. The analysis unit allows further image analysis and also provides the user interface for command and control of the instrument.

Events are defined by hardwired coincidence requirements between the  $X$  and  $Y$  array outputs so as to minimize the load on the digital system. Through this design it is expected that the limit on count rate will be not set by the hardware but by random coincidence background, which is exacerbated by the slowness of the light output from the ZnS:Ag screen. To reduce the coincidence background, a recently developed boron-rich liquid scintillator [18] is being examined as a long term replacement for the ZnS:Ag. It is substantially faster than the ZnS:Ag and appears to be inexpensive and easy to fabricate into imaging planes.

## 2.2. Neutron Source

The neutron source for the prototype instrument is a  $^{252}\text{Cf}$  source with a total intensity of  $2 \times 10^6$  n/s, uniformly distributed over the planar area of the detector ( $40 \text{ cm} \times 40 \text{ cm}$ ). The source strength was chosen to provide reasonable detection times, while minimizing radiation exposure to the operator. A uniform source close to the detector plane ensures that all portions of the active area of the detector have a similar response function and are used to form the image. This minimizes the counting time to achieve a given statistical confidence level across the entire inspection area. Besides increasing mine detection speed, minimizing measurement time decreases operator radiation exposure. Finally, the source geometry produces as homogeneous a background as possible, thus facilitating image analysis. In fact, precise uniformity is not necessary as long as the two dimensional

response function is, as expected, reproducible for a given set of soil conditions.

There are other possible choices for an isotopic neutron emitter that could be made in a uniform continuous sheet or array of distributed sources. Among the factors to be considered are half life, specific activity and neutron energy. The half lives of  $^{252}\text{Cf}$ ,  $^{241}\text{Am}$  and  $^{210}\text{Po}$  are all acceptable for a practical system (2.46 years, 433 years and 138 days respectively). The latter two are  $\alpha$  emitters that are commonly used with the  $^9\text{Be}(\alpha, n)$  reaction. The albedo intensity,  $I$ , is a measure of the total thermal neutron flux returning from the area of interrogation. Let  $B_i$  be the rate per source neutron of thermal neutrons detected at the  $i$ th pixel of the imager, without a target present. The albedo intensity, which is a function of the moderating properties of the soil, is then defined as

$$I = \sum_i B_i \quad (1)$$

where the summation is over a  $2 \times 2$  grid of central pixels of the image array. The albedo intensity as a function of incident neutron energy, estimated by Monte Carlo simulation, is shown in Figure 4 for the geometry of Figures 1 and 2, with a 500 g cylinder of C4 explosive buried 5 cm under sand with 3 and 10% water content. The detector plane is 1 cm above the soil surface. (Details of the geometry and simulation are given in Subsection 3.1.) At each point on both curves, a monochromatic neutron source is assumed. A

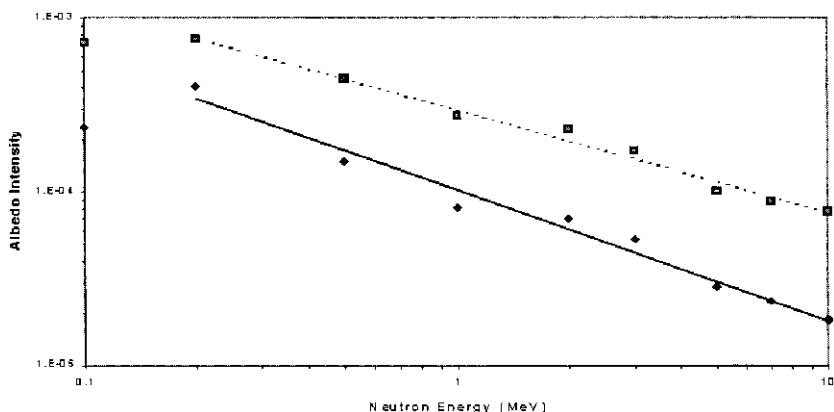


**Figure 4.** Albedo intensity (Eq. (1)) vs. incident neutron energy, estimated from Monte Carlo simulations for the land mine detector of Figures 1 and 2. The detailed geometry is described in Subsection 3.1. Lower curve is for a medium of sand + 3% water. Upper curve is for sand + 10% water.

least squares fit to the curves reveals that the albedo intensity decreases with increasing neutron energy  $E_n$  according to:

$$\begin{aligned} I &\approx 1.0 \times 10^{-4} E_n^{-0.72} && 3\% \text{ water content} \\ I &\approx 3.0 \times 10^{-4} E_n^{-0.62} && 10\% \text{ water content} \end{aligned} \quad (2)$$

To maximize signal, this would suggest that a lower energy spectrum, provided by  $^{252}\text{Cf}$  or the  $^{19}\text{F}(\alpha, n)$  reaction would be preferred. The geometry assumed a land mine buried at a depth of 5 cm. For deeper mines, a higher neutron energy, such as that of the  $^9\text{Be}(\alpha, n)$  reaction, would be preferred, since the neutrons would penetrate further into the soil and the spectrum near the mine would be softened by the soil above the mine.

Uniform spatial coverage could be achieved in a number of ways. The simplest is a square grid of point sources. Figure 5 shows the distribution of neutron flux density per unit source activity (n/s/cm<sup>2</sup>) in the plane of the ground/air interface for three different arrays of point isotopic neutron sources. Sources are equally spaced, with spacings of 5, 6.67 or 10 cm (cf. the 6.5 cm minimum diameter of an AP mine), in a 40 cm  $\times$  40 cm square grid in the plane of the imager. A 5 cm standoff between the imager plane and the ground is assumed. It appears that, for a standoff of 5 cm, a 5  $\times$  5 array of 40 ng  $^{252}\text{Cf}$  sources with 10 cm spacing could adequately approximate, with acceptable flux peak-to-valley ratios, the neutron spatial distribution of a continuous uniform source. Calculations have shown that the source spacing should scale with the detector standoff, which implies that if a 2.5 cm standoff is desired, four times as many sources are required to keep the flux distribution acceptably smooth. The cost of so many sources would be high and handling would be complex. It may also be difficult to manufacture such small point sources.

A uniform, continuous, thin sheet  $^{252}\text{Cf}$  source is the preferred approach for the proof-of-principle instrument. The biggest problem is that the physical quantity of  $^{252}\text{Cf}$  is very small ( $\sim 1 \mu\text{g}$ ) and the area density is minute ( $\sim 0.6 \text{ ng/cm}^2$ ). Fortunately, there are companies that specialize in making  $^{252}\text{Cf}$  fission foil sources having similar concentrations. They can make a source of the size necessary to cover the 0.16 m<sup>2</sup> area, either in one piece or as a mosaic of smaller sheets, at a reasonable cost. A detector using a conventional isotopic source would require shielding for transport and shipping, but not necessarily operation (due to the standoff of operator's station from instrument head). This is the approach that is being taken for the prototype. Designs are presently being completed and a manufacturing contract will soon be let.

The conventional isotopic source has a few logistical disadvantages, which could be eliminated by switchable (on/off) neutron source: (1) It

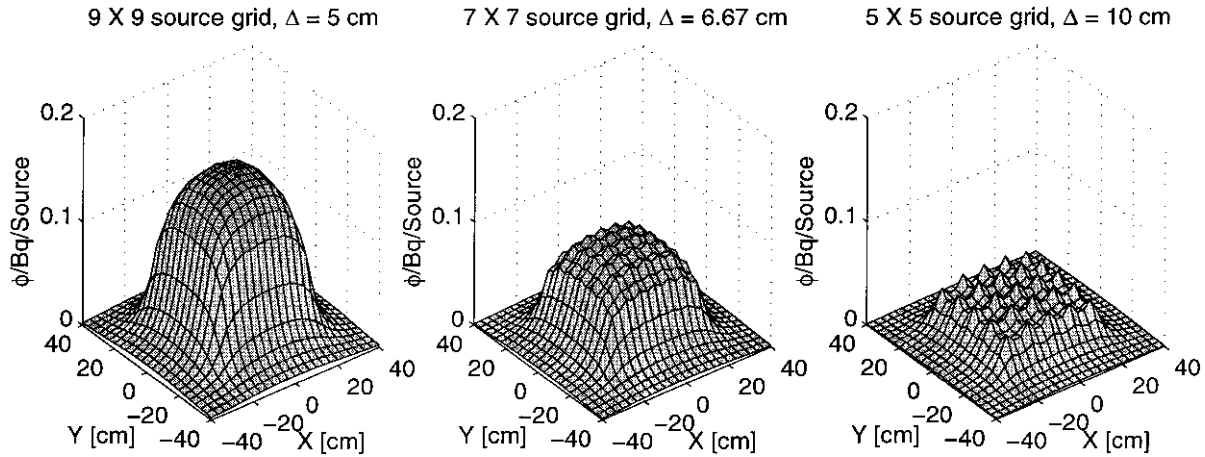


**Figure 5.** Distribution of neutron flux density per unit source activity,  $\phi$  ( $\text{n}/\text{s}/\text{cm}^2$ ) in the plane of the ground–air interface for three different arrays of point isotopic neutron sources. Sources are equally spaced, with spacing  $\Delta$  cm, in a  $40\text{ cm} \times 40\text{ cm}$  square grid in the plane of the imager. A 5 cm standoff between the detector plane and the ground is assumed.

is always emitting radiation (neutrons and gamma rays), which presents a perceived hazard to the operator. (2) It complicates operating procedures, as it must be shielded when not in use, when the operator is nearby and in transport. (3) It creates logistic problems because of the burden generated by military and civilian regulatory agencies. There are several methods of switching an isotopic neutron source on and off. The most promising is an  $(\alpha, n)$  source, switched by binary component separation. Many issues need to be analyzed, including separation methods, weight, yield, safety and ease and cost of fabrication. This will be a subject of future work.

An electronic neutron generator would be an alternative way to achieve a switchable source and it could improve image contrast. The thermal neutron decay time constant ( $1/e$ ) is  $300 \mu\text{s}$  for soil with high moisture content and  $600 \mu\text{s}$  for low moisture soil. This is substantially different from the decay constant of TNT ( $160 \mu\text{s}$ ), due to the large ( $1.78 \text{ b}$ ) thermal neutron absorption cross section of nitrogen. Thus, measurement of thermalization decay constants can dramatically increase the soil/mine contrast [1]. This would be expected to improve performance the most in high moisture soil. A compact, pulsed electronic neutron generator which provides a uniform, low flux ( $\sim 600 \text{ n/cm}^2/\text{s}$ ), distributed across a broad ( $40 \text{ cm} \times 40 \text{ cm}$ ) area, would be a suitable switched neutron source whose pulses would allow measurement of the thermal decay constants. No such generators presently exist.

There are various portable, sealed tube deuterium–deuterium (D-D) and deuterium–tritium (D-T) neutron generators, based on different principles [19,20], that are commercially available for a number of industrial applications. They provide intense outputs ( $10^8$ – $10^{11} \text{ n/s}$ ) and have relatively compact designs. However, their inherent designs are based on a single target and ion source types that do not allow them to be readily adapted to provide a uniform, low flux, distributed across a broad area. We have developed several novel design concepts that capitalize on the low neutron output per unit area needed for this application. It should be noted that, although switchable sources are attractive from the logistics, they are not necessary for the success of the detector. Development of switchable sources is challenging and expensive and will be a subject of future work.

### 3. Modeling Studies

#### 3.1. Method

To determine the efficacy of the imager in a mine detection role, it is necessary to estimate the target-to-background contrast as a function of a number of varying parameters. The detector signal is sufficiently high

that electronic noise can be eliminated using a threshold. The statistical uncertainty in the target-to-background contrast is thus determined by the Poisson statistics of detected neutrons over the target and from background soil. The contrast is related to the backscattered thermal neutron rate, which can be systematically studied using modern Monte Carlo modeling techniques, prior to fabricating a detector. The modeling code chosen was the MCNP neutron transport code developed by the Los Alamos Nuclear Laboratory [21]. It is probably the most respected and most widely used program of its kind and it has been verified extensively by nuclear researchers in both complicated and simple geometries. For what follows, a standard geometry was defined to be 500 g of C4 explosive buried at a depth (distance from soil surface to top of mine) of 5 cm with the detector array 1 cm above the ground surface. The standard geometry is typical of a large AP mine. (In very rough terms, a small AP mine has <100 g of explosive, a medium AP mine has about 100–200 g and a large one has about 400–500 g. A small AT mine has about 2 kg of explosive, a medium AT mine has about 6–7 kg and a large one has about 10–13 kg.) The detector array was approximated by a  $40 \times 40$  array of 1 cm square pixels. The detector response to thermal neutrons was assumed to be ideal. The source was a uniform sheet of  $^{252}\text{Cf}$ , with the same dimensions as the detector, seated immediately above the detector plane and concentric with the detector array. The total source intensity was  $2 \times 10^6$  n/s. The target was a right circular cylinder of solid explosive material, having height equal to diameter and center directly under the array center. All results which follow are for the standard geometry, except as noted.

For the Monte Carlo modelling studies, the albedo signal (per pixel)  $A_i$  is a measure of target-to-background contrast. It is defined as

$$A_i = (S_i - B_i)/B_i \quad (3)$$

where  $S_i$  is the count rate per source neutron for pixel  $i$  with the target (explosive block) in place and  $B_i$  is defined in Eq. (1). Results are presented for variations in the moisture content of the soil, explosive mass, depth of burial of the land mine, type of explosives, presence of other common materials, the height above ground of the detector (standoff) and height variation of the ground surface. In what follows, one dimensional graphs of albedo signal represent an average over a  $4 \times 4$  grid of pixels concentric with the detector array. The grid size was chosen so that the smallest object of interest placed at the center would completely fill those pixels and hence the response due to the pure target could be calculated. A small AP mine (diameter  $\sim 6.5$  cm) will completely cover a  $5 \times 5$  grid and will partially cover about another 24 pixels.

### 3.2. Parametric Variation of Albedo Signal

Hydrogen content, primarily due to water, is the primary determinant of the albedo properties of soil. Figure 6 shows the variation of albedo intensity with water content in sand (pure  $\text{SiO}_2$ ). The graph extends to 20% because the realistic range of soil water content is between 0 and 30% (w/w) water for various soils from sand through loam to clay [1]. (Although saturation levels are quoted as high as 50%, we were unable to exceed 25% in experiments with sand.) The upper curve is for a  $^{252}\text{Cf}$  source. Above about 2% water content, the intensity is roughly linear with water content. The lower curve is for an Am–Be source. The trend is similar, but the intensity per source neutron is about 1/2 of that for Cf. Similar results are obtained for more complex ANSI soil, if plotted against total hydrogen content.

As previously stated, soil moisture decreases the albedo signal from explosives. Figure 7 shows the variation of the albedo signal for the standard geometry as a function of the percentage water content in sand. The signal is significantly above 100% in dry conditions and falls asymptotically to ~2% for near saturation.

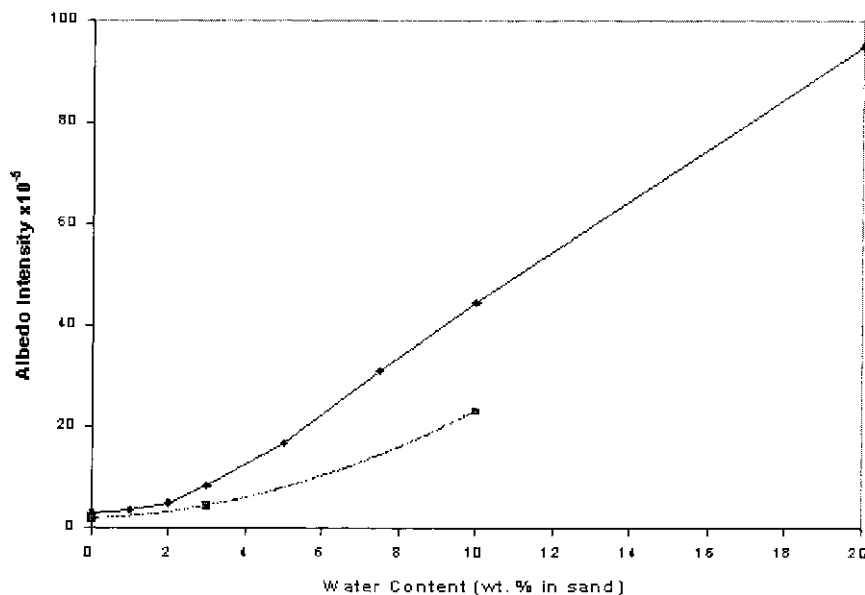


**Figure 6.** Variation of albedo intensity (Eq. (1)) with water content in sand. Upper curve is for  $^{252}\text{Cf}$  source. Lower curve is for Am–Be source. Graphs are calculated from Monte Carlo simulations for the land mine geometry described in Subsection 3.1.

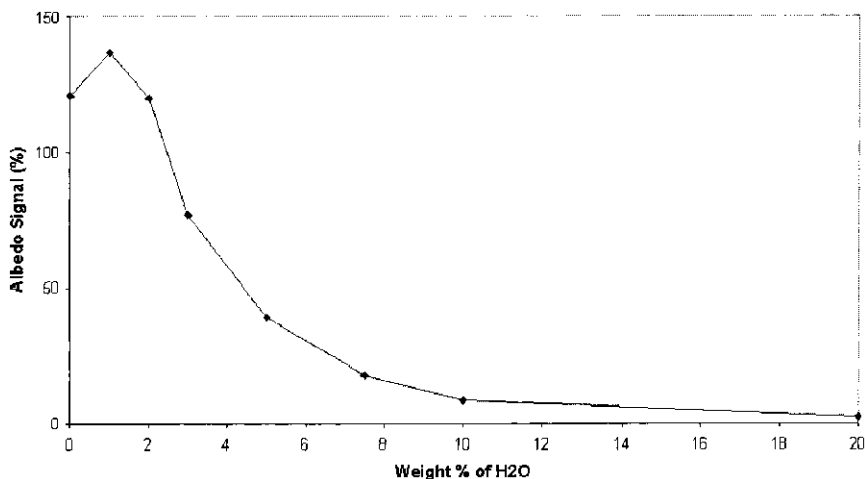


**Figure 7.** Variation of albedo signal (Eq. (3)) with water content in sand. Source is  $^{252}\text{Cf}$ . Graph is calculated from Monte Carlo simulations for the land mine geometry described in Subsection 3.1.

The albedo signal was calculated for 100, 500, and 1000 g of C4, corresponding respectively to a small to medium AP, large AP, and small AT mine, using the standard geometry in sand, with 0, 3, and 10% water content. For 0 and 3% water, the albedo signal,  $A$  (expressed in %), was found to increase linearly with explosive mass,  $M(\text{g})$ , to within a few percent error,

$$\begin{aligned} A &= 0.24M && 0\% \text{ water content} \\ A &= 0.14M && 3\% \text{ water content} \end{aligned} \quad (4)$$

For a 10% water content, the trend appears nonlinear (Figure 8), but the errors on the calculations are much larger. This suggests that care should be exercised when extrapolating results to small explosive masses in wet soil.

The variation of the albedo signal with depth of burial of the land mine was studied for the standard geometry in dry sand and sand with 3 and 10% moisture. The decrease in signal with depth was less than exponential. For larger mines and drier conditions, a substantial albedo signal remained at more than 15 cm depth. For higher moisture contents, a usable signal still remained at more than 15 cm depth. An example of the depth variation for a PMA2 land mine, which is much smaller than the standard geometry mine ( $\sim 100$  g versus 500 g), is shown in Figure 9.

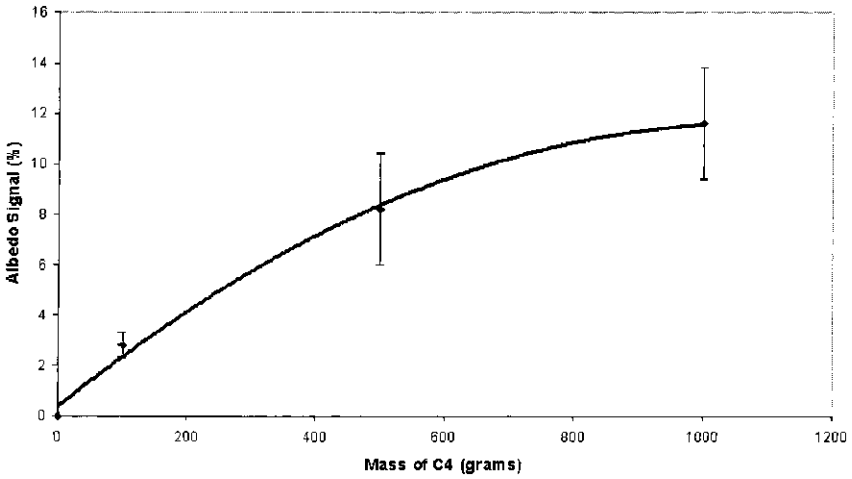


**Figure 8.** Variation of albedo signal (Eq. (3)) with mass of C4 explosive in sand + 10% water. Graph is calculated from Monte Carlo simulations for the land mine geometry described in Subsection 3.1.

Neutron albedo imaging relies on detecting increased neutron moderation, caused by a locally elevated concentration of hydrogen from explosives. It is important, then, to examine the hydrogen content of explosives with respect to soil and common environmental materials. Table 1 shows

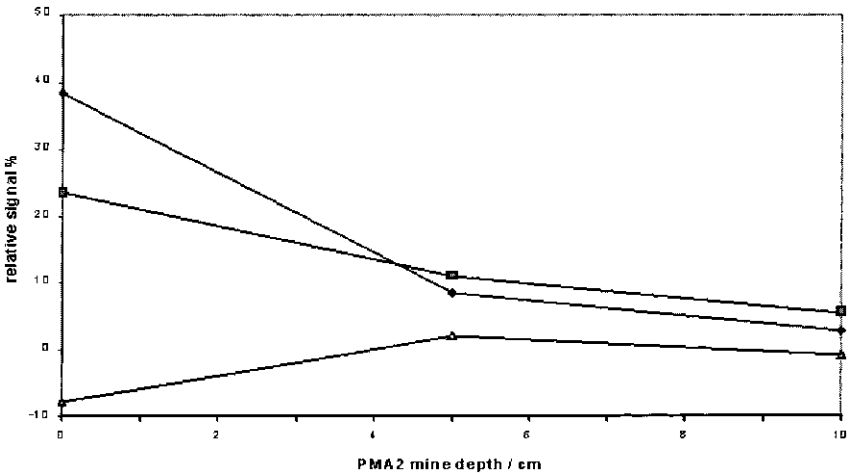


**Figure 9.** Predicted albedo signal (Eq. (3)) vs. depth from a PMA 2 land mine in dry sand (diamonds) and sand with 3% water (squares) and 10% water (triangles). Graph is calculated from Monte Carlo simulations for the land mine geometry described in Subsection 3.1.

**Table 1. Hydrogen Content of Explosives and Other Materials**

Material	H (atoms/cm <sub>3</sub> × 10 <sup>-22</sup> )
Dry Sand	0
Sand + 3% H <sub>2</sub> O	0.363
Sand + 10% H <sub>2</sub> O	1.21
ANSI soil	0.98
C4	3.57
TNT	2.16
RDX	2.52
PETN	2.54
NH <sub>4</sub> NO <sub>3</sub>	5.12
Dynamite	3.01
Wood (dry)	2.65
Wood (wet)	4.66
Lucite	6.36
PVC	3.84
Polyethylene	7.83
H <sub>2</sub> O	6.68

the hydrogen content of some soils, explosives and materials which might be present in the ground. Monte Carlo calculations of the albedo signal of some of these materials, using the standard geometry, are shown in Table 2 for sand with 0%, 3%, and 10% moisture. When plotted, the albedo signal, as expected, increases with increasing hydrogen concentration contrast (Figures 10, 11, and 12). Least squares fitting shows that the albedo signal increases linearly for moist soil, but has a cubic relationship for dry soil. The albedo signal,  $A$  (%), is given by

$$\begin{aligned}
 A &= (-11.379 \pm 2.046)H + (15.424 \pm 0.762)H^2 \\
 &\quad + (-0.998 \pm 0.067)H^3 \quad \text{0% water content} \\
 A &= (25.613 \pm 0.107)H \quad \text{3% water content} \\
 A &= (3.583 \pm 0.096)H \quad \text{10% water content} \quad (5)
 \end{aligned}$$

where  $H$  is the hydrogen contrast (difference between hydrogen concentration of target and that of the embedding medium in units of atoms/cm<sup>3</sup> × 10<sup>-22</sup>). The average residuals are 5.2, 3.8, and 1.8 (units of % albedo) for 0, 3, and 10% moisture respectively. These relationships should allow extrapolation to other buried objects from the results shown in this section for C4.

The standard geometry assumes a 1 cm standoff (height of detector plane above ground surface). Since this may not always be possible, the

Table 2. Albedo Signal (Equation 3) Expressed in % for Explosives and Other Materials<sup>a</sup>

Material	Sand + 0% H <sub>2</sub> O	Sand + 3% H <sub>2</sub> O	Sand + 10% H <sub>2</sub> O
PETN	61	51	5.0
NH <sub>4</sub> NO <sub>3</sub>	207	120	12
H <sub>2</sub> O	314	166	20
Wood (dry)	51	53	7.0
Wood (wet)	188	114	15
Polyethylene	378	190	22
Aluminum	-4	-5.6	-6.9
Void	-1.7	-6.9	-5.9

<sup>a</sup>Monte Carlo simulations with the standard geometry of Subsection 3.1 were used to estimate the albedo signal.

variation of albedo signal with standoff was examined. Figure 13 shows that the albedo signal decreases in a weak exponential manner with standoff, that is, as  $e^{-\beta h}$  where  $h$  is the standoff in cm and  $\beta$  is a constant which differs for each moisture level. The value of  $\beta$  is roughly 0.28 for 0% moisture and 0.14 for 3% moisture. For 10% moisture, there are different values of  $\beta$  for  $h < 2$ ,  $2 < h \leq 7.5$ , and  $h > 7.5$ . The signal generally decreases by about a factor of 2 for a 4 cm increase in standoff. This suggests that the standoff should be minimized, although the detector could function at reduced sensitivity if the standoff were increased by a few cm. This result also emphasizes

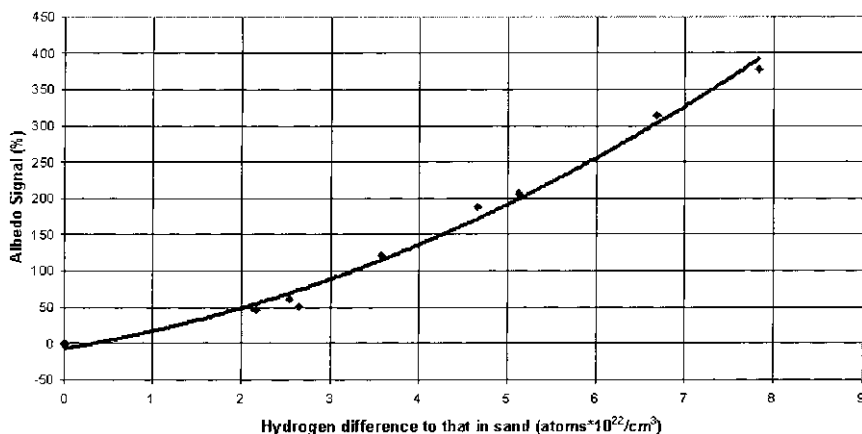
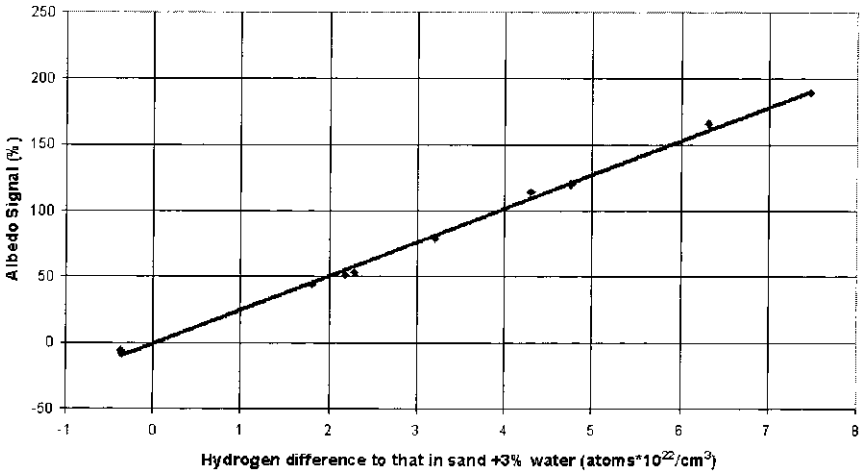
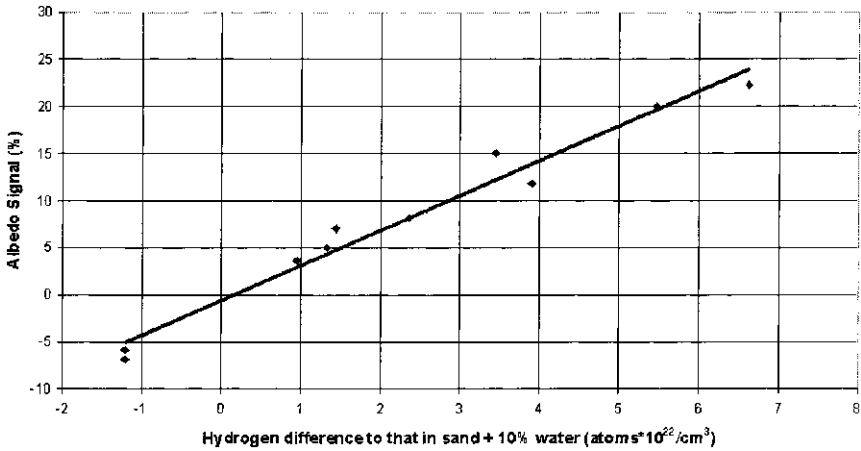


Figure 10. Variation of albedo signal (Eq. (3)) vs. hydrogen concentration contrast for various materials in dry sand. Graph is calculated from Monte Carlo simulations for the land mine geometry described in Subsection 3.1.



**Figure 11.** Variation of albedo signal (Eq. (3)) vs. hydrogen concentration contrast for various materials in sand + 3% water. Graph is calculated from Monte Carlo simulations for the land mine geometry described in Subsection 3.1.



**Figure 12.** Variation of albedo signal (Eq. 3) vs. hydrogen concentration contrast for various materials in sand + 10% water. Graph is calculated from Monte Carlo simulations for the land mine geometry described in Subsection 3.1.

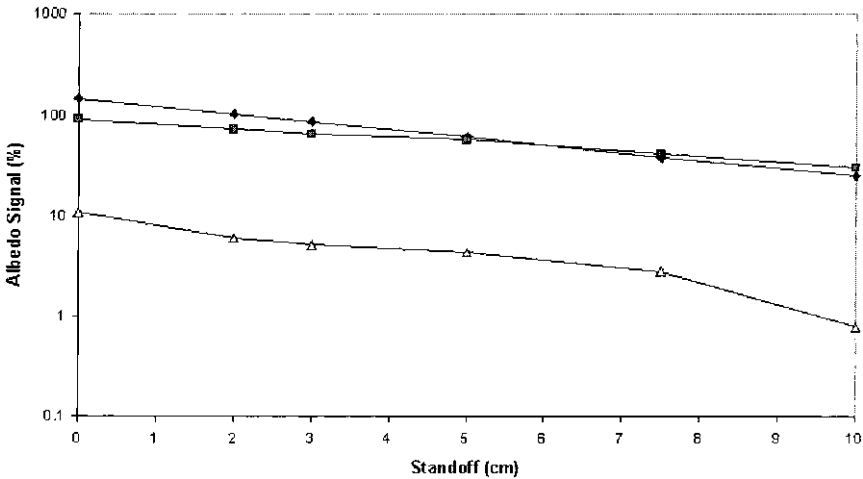


**Figure 13.** Variation of albedo signal (Eq. (3)) with detector standoff (height of detector plane above ground surface). Variations are shown for dry sand (diamonds) and sand with 3% water (squares) and 10% water (triangles). Graphs are calculated from Monte Carlo simulations for the land mine geometry described in Subsection 3.1.

the advantage of imaging in neutron albedo detection of land mines. For point detection, since the albedo signal (contrast) changes with standoff, one needs to know and correct for standoff to infer material properties from albedo measurements. In imaging, the contrast may change with standoff, but the shape of a contrast anomaly will not. This makes imaging much more tolerant to small changes in standoff.

The data from Figure 13 can also be used to gain insight into the effect of ground surface roughness. For a fixed average detector height, the change in albedo signal for a given change in detector height was estimated. Since the signal in Figure 13 is an average over a small portion of the array (4 cm  $\times$  4 cm) which looks at a homogeneous region, the change in albedo signal due to a variation in detector standoff should be roughly the same as the change in albedo signal due to the same size surface height variation, for a constant detector height. The variation in albedo signal vs. variation in ground surface height and sand moisture content is presented in Table 3 for the “standard” detector standoff of 1 cm and a standoff of 2 cm. The percentage uncertainties in albedo estimation range from 6 to 12% for a 0.5 cm surface height standard deviation and from 12 to 24% for a 1.0 cm surface height standard deviation. Examination of Eq. (5) reveal that the percentage error in hydrogen estimation is equal to percentage error in albedo estimation for sand with 3 and 10% water and approximately equal

**Table 3. Variation in Neutron Albedo Signal vs. Variation in Ground Surface Height and Sand Moisture Content<sup>a</sup>**

Moisture (%)	Average albedo signal (%) $\pm$ Standard deviation			
	Detector height = 1.0 cm		Detector height = 2.0 cm	
	$\sigma = 0.5$ cm	$\sigma = 1.0$ cm	$\sigma = 0.5$ cm	$\sigma = 1.0$ cm
0	130.5 $\pm$ 15.4	130.5 $\pm$ 30.9	103.2 $\pm$ 12.1	103.2 $\pm$ 24.5
3	88.7 $\pm$ 5.3	88.7 $\pm$ 10.7	78.7 $\pm$ 4.7	78.7 $\pm$ 9.4
10	7.5 $\pm$ 0.9	7.5 $\pm$ 1.7	6.5 $\pm$ 0.5	6.5 $\pm$ 0.9

<sup>a</sup>Method of calculation is found in Subsection 3.2.  $\sigma$  is the standard deviation of the ground variation. Results for both the standard geometry detector standoff of 1cm and a standoff of 2cm are shown.

for dry sand. By examining Table 1, it can be seen that these uncertainties would not interfere with distinguishing any of the explosives from any of the soils. Dry wood could be confused with RDX and PETN. However, since an image is being formed, the surface height variation could easily be distinguished from mine shapes by the difference in spatial variation (barring pathological cases where roughness occurs in patches that are the same shape and size as mines). This reemphasizes the advantages of imaging the neutron albedo distribution vs. making point measurements.

### 3.3. Spatial Distribution

To study image properties of the detector, calculations were performed for a 1 kg vertical cylinder (9.54 cm diameter, 8.46 cm height) of C4 at a depth of 5 cm in sand with 0, 1, 3, and 10% moisture. Two dimensional distributions of the fractional albedo signal in the horizontal ( $XY$ ) plane are shown in Figures 14, 15, 16, and 17. The horizontal area shown is 20 cm  $\times$  20 cm (1/2 the field of view of the imager), with 2 cm pixels.

The maximum signal is comparable for 0, 1, and 3% water content. The signal for 10% water content is much smaller and is statistics-limited. The peak signals are in general agreement with Figure 7. The diameter of the central peak of the signal (full width at half maximum) in dry sand is  $\approx$  5–6 pixels (10–12 cm), which is comparable to the diameter of the cylinder of explosives. With increasing moisture, the width of the central region expands and the albedo signal strength spreads further from the center, extending well beyond the displayed region.

Smaller explosive masses are expected to have similar spatial distribution properties, if normalized to the maximum albedo signal. Although the distribution also broadens with increasing depth of burial, it may be possible to separate this effect from that of increased moisture through a

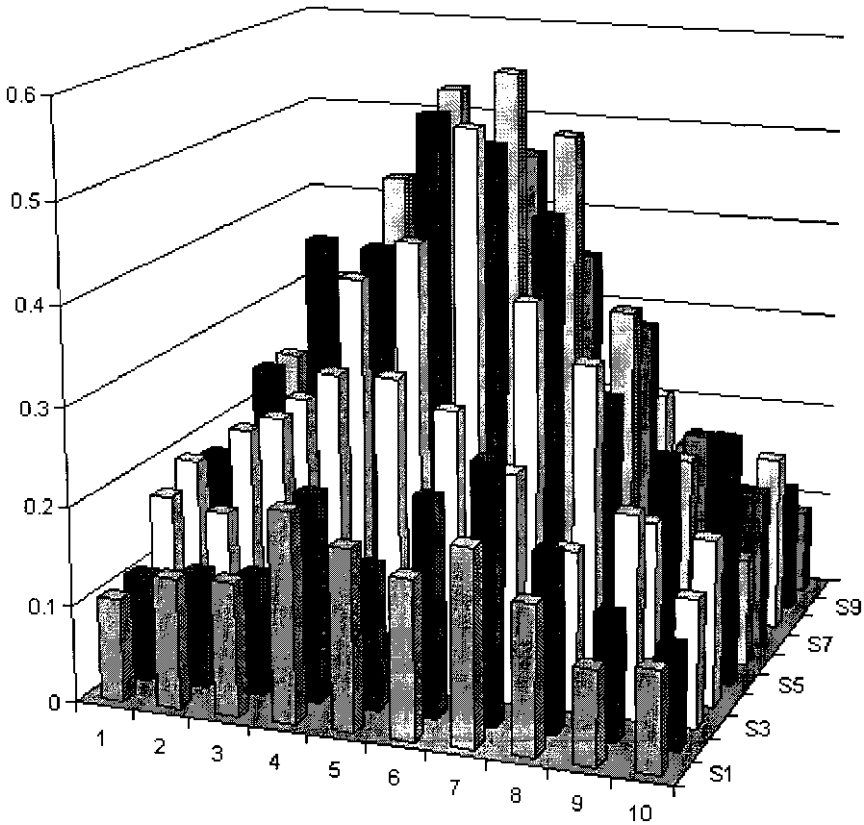


**Figure 14.** Two dimensional distribution of the fractional albedo signal (Eq. (3)) in the horizontal ( $X, Y$ ) plane in dry sand over a 1 kg cylinder of C4 (~10 cm diameter). Land mine is 5 cm below the center of grid coordinate (5,S5). Horizontal extent is 20 cm  $\times$  20 cm (1/2 FOV of the imager) and spacing between horizontal tick marks is 2 cm. Graph is calculated from Monte Carlo simulations for the land mine geometry described in Subsection 3.1.

knowledge of the moisture content. The latter can be estimated from the albedo intensity (Figure 6).

The computer modeling suggests that examination of the strength of the albedo signal, its spatial distribution and the albedo intensity can provide estimates of the size, shape and depth of suspicious objects. However, the model geometry used has made a number of simplifying assumptions, notably ideal detector response, simple targets and uniform soil. In practice, complicated land mine structure (including voids), non-uniform soil and typical detector response characteristics can cause the albedo images to differ substantially from the model. Thus, in order to determine the optimum

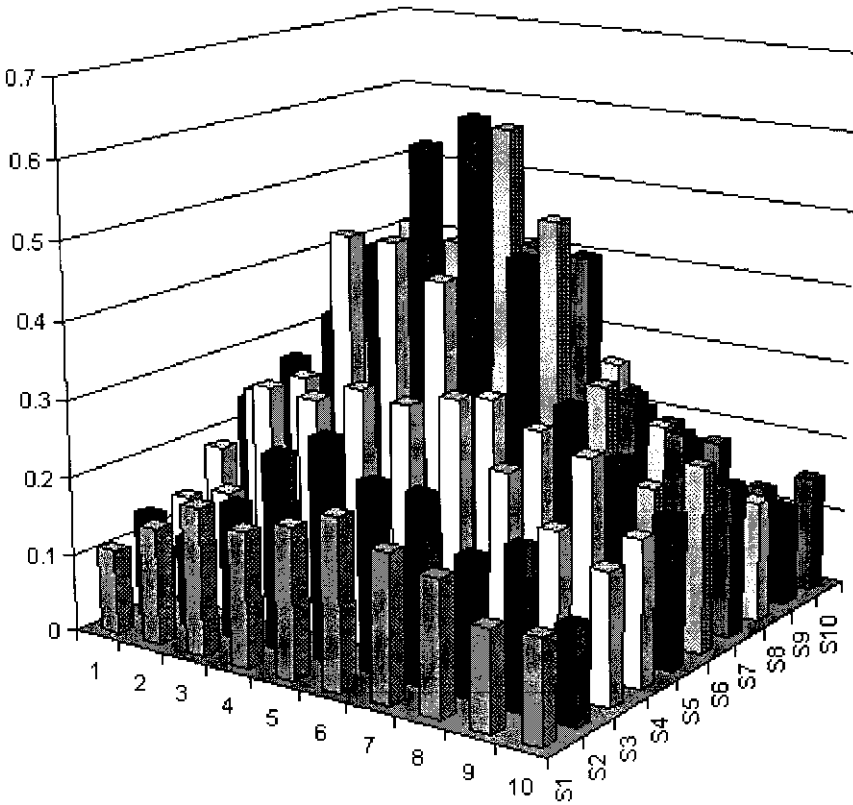


**Figure 15.** Two dimensional distribution of the fractional albedo signal (Eq. 3) in the horizontal ( $X, Y$ ) plane in sand + 1% water over a 1 kg cylinder of C4 (~10 cm diameter). Land mine is 5 cm below the center of grid coordinate (5, S5). Horizontal extent is 20 cm  $\times$  20 cm (1/2 FOV of the imager) and spacing between horizontal tick marks is 2 cm. Graph is calculated from Monte Carlo simulations for the land mine geometry described in Subsection 3.1.

method of analysis and to completely characterize the performance of the imager, detailed data must be acquired using a prototype instrument under a wide range of conditions.

#### 4. Performance

The previously described model can be used to investigate the effect of three main parameters in instrument performance; spatial resolution, imaging time and albedo signal strength. Figures 14, 15, 16, and 17 show that the instrumental resolution of 1 cm  $\times$  1 cm should be more than

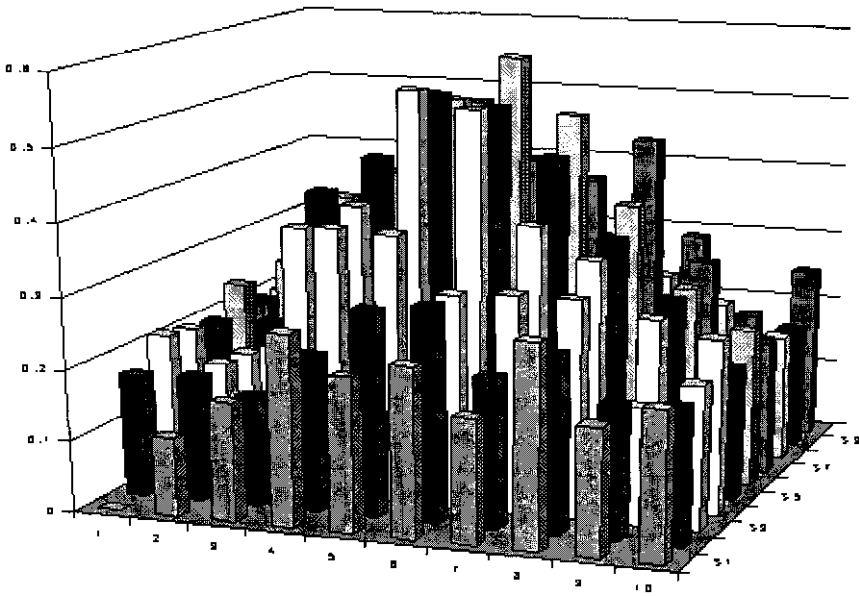


**Figure 16.** Two dimensional distribution of the fractional albedo signal (Eq. 3) in the horizontal ( $X, Y$ ) plane in sand + 3% water over a 1 kg cylinder of C4 (~10 cm diameter). Land mine is 5 cm below the center of grid coordinate (5, S5). Horizontal extent is 20 cm  $\times$  20 cm (1/2 FOV of the imager) and spacing between horizontal tick marks is 2 cm. Graph is calculated from Monte Carlo simulations for the land mine geometry described in Subsection 3.1.

adequate to accurately image the two dimensional distribution of the albedo signal over a land mine.

To estimate the time to detect a target, it is instructive to look at a simple detection algorithm which alarms if the albedo signal in an appropriately sized area of the detector exceeds a threshold. It is assumed that the albedo signal is normally distributed. This is reasonable, since the detector is operating in photon counting mode. (The PMT pulses from neutron events are large enough to be easily distinguished from electronic noise by setting a discriminator level.) The albedo signal is a ratio of Poisson-distributed numbers which is well approximated by a normal distribution as long as total counts are not too small. We will choose the detection threshold to be  $m$  standard deviations of the albedo signal. For small albedo signals (<10%), it is straightforward to calculate the minimum counting time,  $T$ , to detect a target. Eq. (3) is first used to estimate the variance in the albedo signal, as a function of the number of background counts, by standard error propagation. Next the albedo signal is equated to  $m$  times the standard

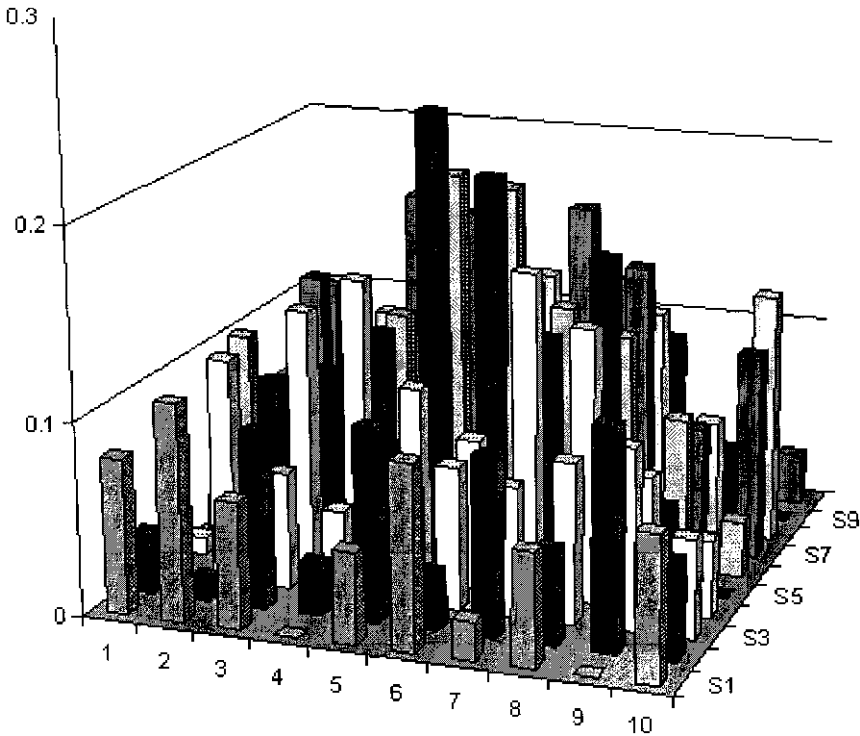


**Figure 17.** Two dimensional distribution of the fractional albedo signal (Eq. 3) in the horizontal ( $X, Y$ ) plane in sand + 10% water over a 1 kg cylinder of C4 (~10 cm diameter). Land mine is 5 cm below the center of grid coordinate (5,S5). Horizontal extent is 20 cm  $\times$  20 cm (1/2 FOV of the imager) and spacing between horizontal tick marks is 2 cm. Graph is calculated from Monte Carlo simulations for the land mine geometry described in Subsection 3.1.

deviation of the albedo signal. Finally, the background counts are expressed as a function of source strength, count time, and average albedo intensity. Combining these results, and with some rearranging,  $T$  is found to be

$$T = \frac{8m^2}{n\bar{A}^2 S \bar{I}} \quad (6)$$

where  $\bar{A}$  is the average albedo signal and  $\bar{I}$  is the average albedo intensity over  $n$  pixels.  $S$  is the total neutron source strength. This assumes that the detection is statistically limited, clutter is not a factor and the detector is 100% efficient. For example, let  $m = 2$  (albedo signal must be two standard deviations greater than 0) and  $n = 16$  (4 cm  $\times$  4 cm area). For the standard geometry of 500 g of C4 buried under 5 cm of sand containing 10% water,

**Table 4. Time to Detect a C4 Cylinder for Various Explosive Masses and Moisture Contents in Sand<sup>a</sup>**

Mass (g)	Moisture (%)	Time (s)
500	0	0.021
500	1	0.012
500	3	0.008
500	10	0.35
100	10	2.85
500	20	1.00

<sup>a</sup>Detection is assumed to be limited by counting statistics rather than clutter. Assumptions are found in Section 4.

$S = 2 \times 10^6$  n/s,  $\bar{A} = 0.08$  (Figures 7, 8) and  $\bar{I} = 4.5 \times 10^{-4}$  per incident neutron (Figure 6). This yields  $T = 0.35$  s. Detection times for the same geometry, with different explosive masses and water contents are shown in Table 4.

Figure 9 shows Monte Carlo calculations of the albedo signal of a PMA2 land mine, buried in sand with 0, 3, and 10% water content, as a function of depth. The PMA2 is a good example of a small to medium size, low metal content land mine. Its main body is a plastic cylinder, 61 mm in height, 68 mm in diameter, containing 100 g of TNT, 35 g of plastic, and roughly 20% void. It is difficult, but not impossible, to detect with a conventional electromagnetic induction mine detector, since it contains only 0.135 g of aluminum. Likewise its small size makes it difficult, but not impossible, to detect with ground penetrating radar. In sand with 0 and 3% water, the albedo signal is positive and decreases monotonically with increasing depth. The PMA2 may be readily detected at all depths up to at least 10 cm. In sand with 10% water, the behavior is more interesting. Presumably because of the internal void space, the signal is negative at zero depth. It increases slowly with depth until a depth of 5 cm and then decreases slowly until at least 10 cm depth. The signal is zero near depths of 3.5 cm and 8.5 cm. At 10 cm, the signal is weak, but measurable ( $\bar{A} \sim -1.8\%$ ). Using the simple detection model of Eq. (6), detection times for different depths of burial and soil moisture contents were calculated (Table 5). For 0 and 3% moisture content, detection times increase with depth. Due to the nonmonotonic nature of the albedo signal vs. depth for 10% moisture (Figure 9), the detection time at 5 cm is greater than that at 0 or 10 cm. There is only a weak dependence on moisture content for flush buried mines. At 5 cm depth, detection time is a minimum at 3% moisture, while at 10 cm depth, detection time decreases with increasing moisture. The latter may seem counterintuitive,

**Table 5. Time to Detect a PMA2 Antipersonnel Land Mine for Various Depths and Moisture Contents in Sand<sup>a</sup>**

Moisture (%)	Detection time (s)		
	Depth (cm)		
	0	5	10
0	0.20	4.86	68.7
3	0.21	1.07	13.4
10	0.33	9.88	6.86

<sup>a</sup>Detection is assumed to be limited by counting statistics rather than clutter. Assumptions are found in Section 4.

but is due to the increase in albedo intensity with increasing moisture (Figure 6). Detection times for flush buried mines are less than 1 s, making slow scanning a possibility for very shallow mines. For depths of 5 and 10 cm, detection times are greater than 1 s and hence the detector is more suitable as a confirmation detector.

The previous performance estimates are based on the uncertainty in estimating the target-to-background contrast, which is dictated by counting statistics. No use is made of the imaging capability of the instrument. Image processing does not improve the target-to-background contrast, but it can improve the target-to-clutter ratio compared to point detectors, which can dramatically improve the probability of detection and false alarm rates. Clutter can be discriminated from land mines on the basis of the horizontal two dimensional spatial distribution (shape) of the albedo signal in conjunction with the strength of the signal. This can be achieved by application of pattern classification techniques to shape features extracted from the albedo signal images or even by visual inspection of the images. Unlike a point detector, an imaging system can reject clutter due to variations in moisture content and vegetative material, by ignoring broad, diffuse signals in favor of compact, mine-sized ones. As discussed in Subsection 3.2, ground surface irregularities also will have less impact on the performance of an imaging detector than on that of a point detector because they will often image as non-compact shapes. The height of a point detector above ground surface must be known in order to compare the albedo signal over an unknown target with a reference background signal. A horizontal planar detector array eliminates this problem, since pixels distant from the target position provide an automatic reference for the detector height. Even if the array is somewhat tilted, the signal change due to the height difference across the array will be gradual and one can compensate for it by inspection or in processing.

In order to illustrate the capabilities of the detector, images of a block of wax, similar in size to a small to medium antipersonnel mine, were obtained. The neutron moderation imager was inverted and the 12.5 cm × 6.5 cm × 3.0 cm, 225 g wax block was placed just above the plane of the imager in various positions. Because the sheet Californium source has not yet been fabricated, an approximation to the source was achieved by suspending a weak ( $10^5$  n/s) Pu–Be source 40 cm above the center of the detector plane. An example albedo signal image is presented in Figure 18, where the block is clearly visible in the lower right-hand corner. Due to the weak, distant source, image acquisition time was 1000 s. It should be emphasized that the images obtained so far are preliminary. They were obtained to test the functioning of the detector and not its performance in mine detection. There is still a significant amount of work to be done to optimize the detector and this optimization, including the sheet neutron source, should significantly improve image acquisition time and image quality.

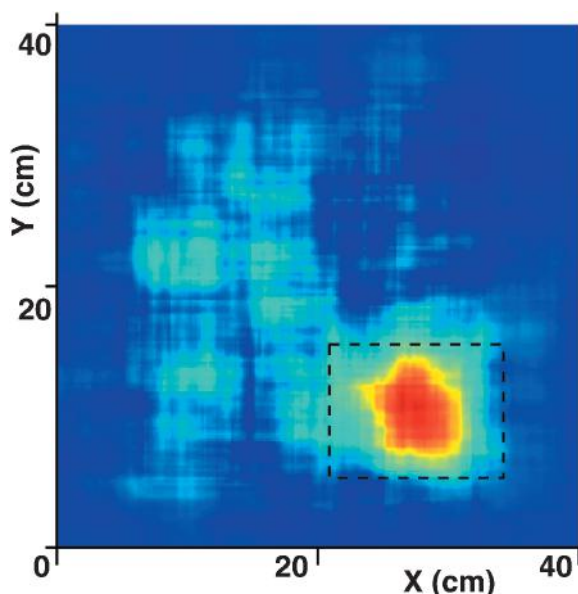


**Figure 18.** Example neutron albedo signal image of a block of wax, similar in size to a small to medium antipersonnel mine, obtained by the neutron moderation imager. The block was placed just above the detector plane. Its position is indicated by the dotted rectangle. The neutron source was a  $10^5$  n/s Pu–Be source suspended 40 cm above the center of the detector plane. Due to the weak, distant source, image acquisition time was 1000 s.

## 5. Conclusions

A conceptual design of a neutron albedo two dimensional imager has been developed. It consists of a novel thermal neutron imaging system, a unique neutron sheet source to uniformly irradiate the underlying ground and hardware and software for image generation and enhancement. A proof-of-principle imager with dimensions of roughly 40 cm  $\times$  40 cm, mass of 13 kg and consuming 10 W of power, has been built, but presently uses a point source offset from the detector plane to approximate a very weak uniform source at the detector plane. Imagery from the detector of mine surrogates was presented.

Realistic Monte Carlo simulations were performed using the same two dimensional neutron imaging geometry as the detector to estimate performance capability, including adequacy of spatial resolution, target-to-background contrast, and detection times. To do so, the strength of the returning neutron signal (relative to background) was determined for various soil and explosive types, moisture contents and other relevant parameters. The simulations showed that the neutron albedo imager is feasible as a land mine detector in a slow scanning or confirmation role. Estimated detection times for flush buried PMA2 AP mines were less than 1 s, making slow scanning a possibility for very shallow mines. For depths of 5 and 10 cm, detection times were greater than 1 s, but no more than about 1 min. Hence the detector is more suitable as a confirmation detector for small mines at greater depths. Larger AP mines (500 g C4 equivalent) buried at 5 cm in 20% moisture content sand could be detected in 1 s. Spatial resolution of the instrument was better than the maximum spatial frequency of the two dimensional neutron distributions. Thus image quality should be sufficient to allow clutter rejection. This should significantly improve detector performance and reduce false alarm rates compared to non-imaging albedo detection, particularly in moist soils, where surface irregularities exist and when the sensor height is uncertain.

Present research is aimed at optimizing the detector and completely characterizing its performance. The sheet Californium source is expected to be installed by summer 2003. Several improvements are also planned which could further enhance the image contrast of land mines and hence improve the detector performance. These include a novel boron-doped liquid scintillator image screen, a broad area pulsed electronic neutron generator and advanced image processing algorithms for automatic target detection, based on pattern recognition and mathematical morphology.

## 6. Acknowledgments

The present work was supported by the Canadian Center for Mine Action Technologies (CCMAT) and Defence R&D Canada.

## References

1. Coleman, W.A. Ginaven, R.O., and Reynolds, G.M., 1974, Nuclear methods of mine detection, vol. III: Technical Report SAI-74-203-L, Science Applications Inc.
2. McFee, J.E. and Das, Y., 1980, The detection of buried explosive objects: *Canad. J. Remote Sensing*, v. 6, p. 104-121.
3. Moler, R.B., 1985, Workshop report: Nuclear techniques for mine detection research, Lake Luzerne, NY, July 22-25, 1985: Technical Report AD-A167968, Army Belvoir Research and Development Center, November 1986.
4. McFee, J.E. and Das, Y., 1991, Advances in the location and identification of hidden explosive objects, Technical Report SR 548, Defence Research Establishment Suffield.
5. Jacobs, A., Dugan, E., Brygoo, S., Ekdahl, D., Houssay, L., and Su, Z., 2002, Lateral migration radiography—a new x-ray backscatter imaging technique: *Penetrating Radiation Systems and Applications IV*, Barber, H.B., Roehrig, H., Doty, F.P., Porter, L.J., and Morton, E.J., eds.: *Proceed. SPIE*, v. 4786, pp. 1-16.
6. Cousins, T., Jones, T.A., Brisson, J.R., McFee, J.E., Jamieson, T.J., Waller, E.J., LeMay, F.J., Ing, H., Clifford, C.E., and Selkirk, B., 1998, The development of a thermal neutron activation (TNA) system as a confirmatory nonmetallic land mine detector: *J. Radioanalyt. Nucl. Chem.*, v. 235, p. 53-58.
7. Clifford, C.E., Ing, H., McFee, J.E., Andrews, H.R., and Cousins, T., 2000, Second generation thermal neutron activation sensor for confirmatory landmine detection: *Transactions of the American Nuclear Society*, v. 82, p. 101-102.
8. McFee, J., Aitken, V., Chesney, R., Das, Y., and Russell, K., 1998, A multisensor, vehicle-mounted, teleoperated mine detector with data fusion: *Detection and Remediation Technologies for Mines and Mine-like Targets III*, Dubey, A.C., Harvey, J.F., and Broach, J.T., eds.: *Proceedings of SPIE*, v. 3392, p. 1082-1093.
9. Haslip, D.S., Cousins, T., Andrews, H.R., Chen, J., Clifford, E.T.H., Ing, H., and McFee, J.E., 2001, DT neutron generator as a source for a thermal neutron activation system for confirmatory land mine detection: *Hard X-Ray and Gamma-Ray Detector Physics III*, R.B.James, Ed., *Proceedings of SPIE*, v. 4507, p. 232-242.
10. Faust, A., 2002, Detection of explosive devices using x-ray backscatter radiation, in *Penetrating Radiation Systems and Applications IV*, Barber, H.B., Roehrig, H., Doty, F.P., Porter, L.J., and Morton, E.J., eds.: *Proceed. SPIE*, v. 4786, pp. 17-28.
11. Church, P., Wort, P., Gagnon, S., and McFee, J., 2001, Performance assessment of an electrical impedance tomography detector for mine-like objects: *Detection and Remediation Technologies for Mines and Mine-like Targets VI*, Dubey, A.C., Harvey, J.F., Broach, J.T., and George, V., eds.: *Proceed. SPIE*, v. 4394, p. 120-131.
12. Garroway, A., Buess, M., Miller, J., Suits, B., Hibbs, A., Barrall, G., Matthews, R., and Burnett, L., 2001, Remote sensing by nuclear quadrupole resonance: *IEEE Transactions on Geosci. Remote Sens.*, v. 6, pp. 1108-1118.
13. Brooks, F.D., Buffler, A., and Allie, M.S., 2001, Landmine detection by neutron backscattering: 7th International Conference on Applications of Nuclear Techniques, Vourvopoulos, G., ed., University of Western Kentucky.
14. Datema, C., Bom, V., and Van Eijk, C., 2000, Landmine detection with neutron backscattering method, in *Nuclear Science Symposium*, October 2000: *Proc. IEEE*, v. 5. p. 5-111-5-114.
15. Gorin, A., Kuroda, K., Manuilov, I., Ryazantsev, A., Morimoto, K., Oku, T., Shimizu, H.M., Suzuki, J., Tokanai, F., Clergeau, J.F., and Guerard, B., 2001, A novel type of position-sensitive detectors for slow neutrons based on wavelength shifting fiber readout: *International Workshop on Position Sensitive Detectors*, Hahn-Meitner Institute, Berlin, pp. 18-19.

16. Hutchinson, D.P., Richards, R.K., Maxey, L.C., Holcomb, D.E., and Cooper, R.G., 2001, Wavelength-shifting fiber readout of scintillation detectors: International Workshop on Position Sensitive Detectors, Hahn-Meitner Institute, Berlin, pp. 23–24.
17. Toh, K., Katagiri, M., Sakasai, K., Matsubayashi, M., Birumachi, A., Takahashi, H., and Nakazawa, M., 2001, High-counting-rate 2-dimensional neutron imaging method using scintillators with wavelength shifting fibers: in International Workshop on Position Sensitive Detectors, Hahn-Meitner Institute, Berlin, pp. 63–64.
18. Vartsky, D., Goldberg, M.B., Shohet, J., Breskin, A., Chechik, R., Guerard, B., and Clergeau, J.F., 2001, Boron rich liquid scintillator for efficient, fast, large area imaging neutron detector, in International Workshop on Position Sensitive Detectors, Hahn-Meitner Institute, Berlin, p. 66.
19. Ethridge, D.R., 1991, Neutron generator tube, U.S. Patent 4,996,017.
20. Gow, J.D. and Ruby, L., 1959, Simple, pulsed neutron source based on crossed-field trapping: *Rev. Sci. Instruments*, v. 30, no. 5, pp. 315.
21. Briemeister, J.F., 1993, MCNP—a general Monte Carlo  $n$ -particle transport code—version 4a: Report LA-12625-M, Los Alamos Laboratory.

# **Resolution Enhancement with Model-Based Frequency Estimation Algorithms in Radar Signal Processing**

**Andreas Stelzer**

Institute for Communications and Information Engineering,  
Johannes Kepler University Linz, Altenberger Str. 69,  
A-4040 Linz, Austria

**Markus Pichler**

Linz Center of Competence in Mechatronics, Altenberger Str. 69,  
A-4040 Linz, Austria

*Received October 25, 2002; revised May 26, 2003*

---

In this work we present results on the improvement of resolution capability and accuracy for radar signal evaluation by means of model-based frequency estimation algorithms. In frequency modulated continuous wave radar sensors, which are widely used in industrial contactless distance measurement applications, the usage of the Fourier Transformation for signal evaluation is very common. Nevertheless, using the Fast Fourier Transformation, the resolution capability for closely spaced targets is limited and directly related to the employed signal bandwidth. Model-based frequency estimation algorithms, developed during the last decades, can essentially improve target resolution and distance accuracy. These improvements are shown on simulation data as well as on measured data. Model order estimation, still a challenge when applying model-based evaluation techniques, is tackled by an adaptive approach.

---

**Key Words.** FMCW, FSCW, frequency estimation, distance measurement, radar resolution, model order estimation.

---

\*To whom all correspondence should be addressed. Phone: +43 70 2468-1858; fax: +43 70 2468-9712; e-mail: a.stelzer@ieee.org. Phone: +43 70 2468-9784; fax: +43 70 2468-9712; e-mail: markus.pichler@lcm.at

## 1. Introduction

Microwave distance sensors based on radar technology are state-of-the-art sensors for contactless measurements in industrial environments due to their insensitivity to most environmental influences even under extreme conditions. Progress in semiconductor technology at higher frequencies is bringing microwave sensors towards applicable products, and further cost reductions necessary for the mass market, e.g. in the automotive industry, are nearly reached.

Besides advances in RF-semiconductor technology, powerful signal processors enable the application of sophisticated signal processing. The Fast Fourier Transformation (FFT) [1] is still by far the most frequently applied algorithm for the evaluation of sensor data measured with a frequency sweep. There are well-known limitations of the FFT, e.g. the resolution limitation of closely spaced targets, which is directly related to the sweep bandwidth. Model-based frequency estimation algorithms are suited to enhance the resolution capability as will be shown in this paper. For model order estimation, typically a challenging task, a new adaptive approach is used.

Beginning with the derivation of the radar signal model, limitations of the FFT will be shown. After describing elementary ideas behind some model-based algorithms, consequences of selecting an incorrect model order are outlined, and the adaptive model order determination procedure is presented. Afterwards, simulation results of the resolution enhancement are shown. Measurement results obtained from a laboratory test setup are presented to verify the improvements achieved with exemplary model-based frequency estimation algorithms [2].

## 2. Radar Signal Model

The radar signal model is derived for a typical radar setup, as shown in Figure 1. The transmit signal is generated by a voltage-controlled

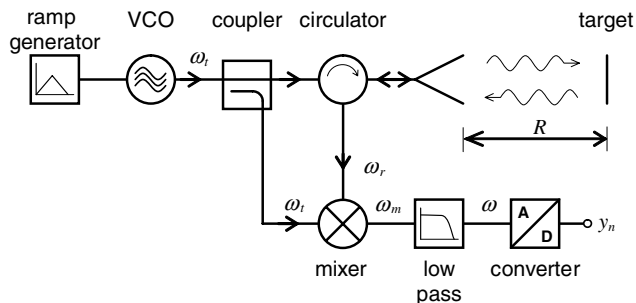


**Figure 1.** Block diagram of an FMCW/FSCW radar setup with a single target at distance  $R$ .

oscillator (VCO). The ramp generator produces either a highly linear ramp for the linear frequency modulated continuous wave (LFMCW) case or small, equal steps in the frequency stepped continuous wave (FSCW) case.

A circulator redirects the received signal to the mixer, where it is mixed with a part of the transmit signal, and low-pass filtered. Finally, this signal is sampled and digitized to values  $y_n$ . Under some constraints, which are mostly fulfilled, the FM and FS case can be viewed as equivalent. The time of flight (TOF) of the electromagnetic wave to the target and back can be expressed by

$$\tau = \frac{2R}{c_0} \tag{1}$$

where  $R$  is the range to the target and  $c_0$  denotes the velocity of light. With a linear modulation scheme the actual transmit frequency becomes

$$\omega_t(t) = \omega_0 + Kt \quad \text{with } K = 2\pi \frac{B}{T} \tag{2}$$

where  $B$  represents the full sweep bandwidth and  $T$  the ramp duration. The propagated wave experiences a phase change during TOF that—under the assumption  $\tau \ll T$ —results in an intermediate frequency (IF) signal phase of

$$\varphi(t) = (\omega_0 + Kt)\tau = \omega_0\tau + Kt\tau \tag{3}$$

Additionally, assuming sampling intervals equidistant in time in the LFMCW case, or equidistant in frequency in the FSCW case, Eq. (3) can, with  $N$  as the number of samples, be rewritten as

$$\varphi_n = \varphi\left(t = \frac{n}{f_s}\right) = \omega_0\tau + 2\pi B\tau \frac{n}{f_s T} = \omega_0\tau + \frac{2\pi B}{N}\tau n = \omega_0\tau + K_{FS}\tau n \tag{4}$$

eliminating time-dependency. In (4)  $K_{FS} = 2\pi B/(f_s T)$  denotes the frequency difference between steps or sampling instants and  $n$  designates the  $n$ -th sample. Thus, for the  $k$ -th individual target at distance  $R_k$  the initial detected phase and the discrete frequency are given by

$$\varphi_{0,k} = \omega_0 \frac{2R_k}{c_0} \quad \text{and} \quad \omega_k = K_{FS} \frac{2R_k}{c_0} \tag{5}$$

respectively. For moving targets the Doppler-shift has to be taken into account, too [3]. Due to the linear behavior of the whole system the response of  $p$  targets is the sum of all individual signals, resulting in a radar signal  $y_n$  which is composed of  $p$  complex exponentials with individual amplitudes  $A_k$ .

$$y_n = \sum_{k=1}^p A_k e^{j(\omega_k n + \varphi_{0,k})} \tag{6}$$

In the radar system sketched in Figure 1 only the real part of the complex IF signal is measured, which results in a sum of cosine functions. With a second mixer and an additional  $90^\circ$  phase shifter in the local oscillator (LO) path, both the inphase (I) and quadrature phase (Q) components of the complex signal can be measured.

### 3. FFT-Based Frequency Estimation

Frequency estimation using the FFT is usually a two-step procedure involving computation of the frequency-domain representation of the sampled data sequence followed by a peak-search in the resulting periodogram. Due to the nature of the FFT which assumes periodicity of the signal in time-domain, the spectrum is evaluated on a grid of fixed frequency values only. As the fineness of the grid is determined by the duration of the sampling period, extending the time-domain data by adding zeros to the available data samples—a procedure known as zero-padding—causes interpolation in a finer frequency-grid, hence facilitating the determination of the exact peak location [4].

The result obtained after padding the time-domain data sequence with zeros is the same as if a long sinusoidal data sequence was multiplied with a rectangular, or boxcar window, which in frequency domain causes the spectrum of the window-function being folded to the location of the sinusoids' frequencies, thus widening the theoretically infinitely narrow spectral peaks. By applying different window-functions, the appearance of spectral peaks in frequency-domain can be controlled and specifically used to reduce sidelobes in the spectrum and therefore influence on other points on the frequency grid.

Two separate performance criteria of frequency estimation algorithms can be distinguished: ranging accuracy and resolution capability. In the following, the term (ranging) accuracy will be used to characterize the deviation of frequency estimates from the respective true values, i.e. how accurately a target's position can be determined. Measurements are always influenced by random noise such as thermal component noise or background clutter, as well as systematic disturbances, e.g. a nonlinear oscillator sweep. Therefore, evaluation results usually contain stochastic and deterministic errors, i.e. a superposition of stochastic deviations over a constant offset. Boundaries for the achievable accuracy under stochastic influences, or more specifically a lower limit on the achievable variance of frequency estimates is given by the Cramér–Rao lower bound (CRB). For the problem on hand, assuming additive white Gaussian noise, the CRB can be computed numerically [5].

Closely spaced peaks in the frequency spectrum usually influence each other and are another source of error in the frequency estimates for the

respective other peaks, yet they may be distinguishable as two peaks. Resolution capability therefore denotes the ability of an algorithm to resolve two closely spaced frequencies in the evaluated signal as two distinct signal components, regardless of possible deviations of the estimates from the true frequency values. Interestingly, in FMCW radar systems the achievable accuracy for a single target can be much better than the minimum frequency distance for which two signal components can be resolved.

The apparent trade-off between accuracy and required computational effort that limits the number of added zeros before computation of the FFT can be overcome in part by noting that in a first-order approximation the topmost spectral values for most window-functions follow a parabola whose parameters and vertex position can be computed in a straightforward manner. Another method to improve estimates is to determine the spectral peak centroid whose location along the frequency axis can be taken as an estimate for the true signal frequency.

Contrary to some common misconception, that like accuracy, resolution can be improved by zero-padding, it is only the finite width of the main lobe of the window function that limits resolution. As the frequency difference between two sinusoids decreases, the corresponding spectral peaks move closer together, and merge to one large peak below a certain limit, inhibiting detection of two sinusoidal components. Interestingly, resolvability at a given frequency difference in the critical region around this limit is largely influenced by the initial phase difference of the two sinusoids. Figure 2 shows

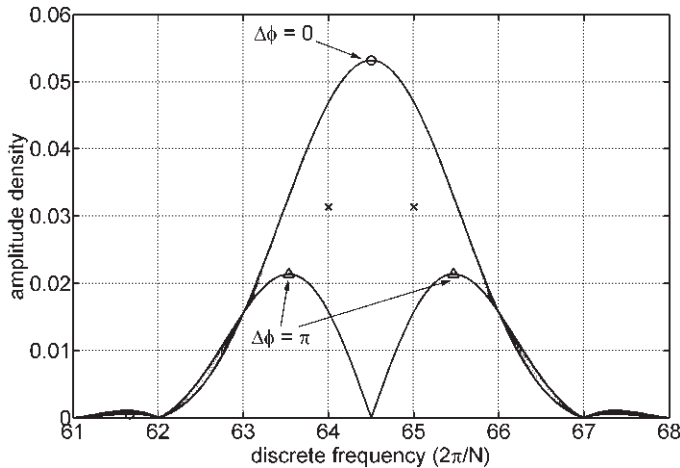


**Figure 2.** FFT spectra for two sinusoids of fixed frequency ( $2\pi 64/256$  and  $2\pi 65/256$  rad/sample) and varying phase difference (in steps of  $\delta\phi = \pi/16$ ) with  $N = 256$  sample points. True peak locations are marked with “x”.

the amplitude density spectra of synthetic signals consisting of two equi-amplitude sinusoids of discrete frequencies  $2\pi 64/256$  and  $2\pi 65/256$  rad/sample, respectively, with an initial phase difference  $\Delta\phi$  varying from 0 to  $2\pi$  in steps of  $\delta\phi = \pi/16$ , as obtained from the FFT after applying a Hanning-window. Apparently, while for certain constellations two peaks are clearly recognizable, in more than half the cases the result contains one large peak instead of two—and the resolution of two sinusoids is impossible. Furthermore, even if two sinusoids are resolved such as in the signal marked with triangles, ranging accuracy is affected as the acquired estimates deviate considerably from the theoretical location indicated by two “x” in the plot.

In an FMCW-system, a limit on resolvable frequency difference means a limit on the distance difference below which two targets cannot be distinguished. In a setup with many closely spaced targets resolution achieved with the FFT frequency estimator may not suffice, necessitating more sophisticated frequency estimation algorithms.

#### 4. Model-Based Frequency Estimation Algorithms

In contrast to FFT analysis, where an unknown signal is decomposed in harmonic components with harmonic frequencies located on a pre-determined grid, model-based analysis utilizes the knowledge of the signal shape of individual target responses and locates signal components at arbitrary frequency values. The results achieved attain or come close to the CRB that may be computed as shown in [5].

According to the radar signal model in (6) a mathematical model of the form

$$s_n = \sum_{k=1}^p c_k e^{j\omega_k n} \quad n=0, \dots, N-1 \quad (7)$$

describing the response of  $p$  independent targets and ideally fitting the measured data  $y_n$  is used for the estimation of the frequencies  $\omega_k$  containing the unknown target distances. The complex amplitudes  $c_k$  also containing the initial phase of the reflections are estimated in a second step. Eq. (7) assumes complex measurement data to fit. In simplified configurations with an inphase measurement branch only, the model order  $p$  must be twice as high as the expected number of targets to fit the real-valued measurement data.

A remarkable property of this signal model is the linear predictability of subsequent samples in forward direction and previous samples in backward direction by means of a linear combination of the  $p$  previous or subsequent sample values [6] (\* denotes complex conjugation).

$$s_n = -\sum_{l=1}^p g_l s_{n-l} \quad \text{and} \quad s_n^* = -\sum_{l=1}^p g_l s_{n+1}^* \tag{8}$$

From this linear predictability property it directly follows via  $z$ -Transformation that the ideal sampled sequence  $s_n$  may be viewed as output of an oscillator in its discrete transfer-function representation, with nonzero initial condition and the zero-sequence as input. If the oscillator is of the order  $M-1 > p$  then there is no unique polynomial representation, leading to a set of  $M-p$  transfer functions given by the reciprocal of the polynomial  $G_l(z)$  defined in (9). Any such oscillator will have  $p$  of its roots on the unit circle in the complex plane, with complex arguments equal to the desired frequency estimates  $\omega_k$ .

$$G_l(z) = \sum_{k=0}^{M-1} g_{k,l} z^{-k} = [1 \quad z^{-1} \quad \dots \quad z^{-(M-1)}] \begin{bmatrix} g_{0,l} \\ g_{1,l} \\ \vdots \\ g_{M-1,l} \end{bmatrix} = \mathbf{z}^T(z) \mathbf{g}_l \tag{9}$$

$l = 1, \dots, M-p$

The vectors  $\mathbf{g}_l$  containing polynomial coefficients  $g_{k,l}$  that form a linearly independent set can be assembled in a full-rank matrix  $\mathbf{\Gamma}$  (10), whose determination, followed by polynomial rooting, is the aim of polynomial-based algorithms.

$$\mathbf{\Gamma} = [\mathbf{g}_1 \quad \mathbf{g}_2 \quad \dots \quad \mathbf{g}_{M-p}] \tag{10}$$

Another view of the problem can be obtained by using the alternate state-space oscillator model of minimum order  $p$  as in (11), with the state-feedback matrix  $\mathbf{A}$ , the state vector  $\mathbf{x}_n$  in the  $n$ -th step, and the output vector  $\mathbf{c}$ . In this case frequencies are contained in the eigenvalues of the matrix  $\mathbf{A}$ .

$$\begin{aligned} \mathbf{x}_{n+1} &= \mathbf{A}\mathbf{x}_n \\ y_n &= \mathbf{c}^T \mathbf{x}_n \end{aligned} \tag{11}$$

For computation of  $\mathbf{A}$ , the extended observability matrix  $\mathbf{\Theta}$  defined in (12) and so-termed for its structure well-known from control theory, can be used. Obviously the state-feedback matrix is a solution to (13), where the notation  $[\cdot]_{[a:b,\cdot]}$  indicates a submatrix containing rows  $a$  through  $b$  only.

$$\mathbf{\Theta} = \begin{bmatrix} \mathbf{c}^T \\ \mathbf{c}^T \mathbf{A} \\ \vdots \\ \mathbf{c}^T \mathbf{A}^{M-1} \end{bmatrix} \tag{12}$$

$$\Theta_{[1:M-1,:]} \mathbf{A} = \Theta_{[2:M,:]} \quad (13)$$

Hence, the frequency estimation problem is transferred to a parameter estimation problem for a linear oscillator.

The model-based algorithms discussed here use either the raw data or the data covariance matrix for frequency estimation. Let  $M \geq p + 1$  ideal data values  $s_n$ , starting at sample position  $n$  be assembled in the data vector  $\mathbf{s}_n$

$$\mathbf{s}_n = [s_n \quad s_{n+1} \quad \cdots \quad s_{n+M-1}]^T \quad (14)$$

Using this notation a noise-free data matrix  $\mathbf{S}$  can be formed by

$$\mathbf{S} = [\mathbf{s}_0 \quad \mathbf{s}_1 \quad \cdots \quad \mathbf{s}_{N-M}] \quad (15)$$

The same notation can be used for the measured values  $y_n$ , to form a measurement data matrix  $\mathbf{Y}$ .

Some algorithms are based on decomposition of the data covariance matrix defined using the expectation operator  $\mathcal{E}\{\cdot\}$  as

$$\mathbf{R}_{ss_m} = \mathcal{E}\{\mathbf{s}_n \mathbf{s}_{n+m}^H\} = \begin{bmatrix} r_{ss_m} & r_{ss_{m+1}} & \cdots & r_{ss_{m+N-1}} \\ r_{ss_{m-1}} & r_{ss_m} & \cdots & r_{ss_{m+N-2}} \\ \vdots & \vdots & \ddots & \vdots \\ r_{ss_{m-(N-1)}} & r_{ss_{m-(N-2)}} & \cdots & r_{ss_m} \end{bmatrix} \quad (16)$$

with entries

$$r_{ss_m} = \mathcal{E}\{s_n s_{n+m}^*\} = \lim_{N \rightarrow \infty} \frac{1}{N} \sum_{n=0}^{N-1} s_n s_{n+m}^* \quad (17)$$

Due to the finite number of available samples  $N$ , the data covariance matrix  $\mathbf{R}_{yy} = \mathbf{R}_{yy0}$  must be replaced by an estimate  $\hat{\mathbf{R}}_{yy}$  in computations, e.g.

$$\hat{\mathbf{R}}_{yy} = \frac{1}{N-M+1} \sum_{k=0}^{N-M} \mathbf{y}_k \mathbf{y}_k^H = \frac{1}{N-M+1} \mathbf{Y} \mathbf{Y}^H \quad (18)$$

Other estimators for this matrix that retain certain properties of the true data covariance matrix such as centrosymmetry may be used instead [7].

For a particular state-space realization given by  $\mathbf{A}_d = \text{diag}\{e^{j\omega_1}, e^{j\omega_2}, \dots, e^{j\omega_p}\}$  and  $\mathbf{c}_d = [1 \ 1 \ \cdots \ 1]^T$ , according to (12) the observability matrix  $\Theta_d$  is of the form

$$\Theta_d = \begin{bmatrix} 1 & 1 & \cdots & 1 \\ e^{j\omega_1} & e^{j\omega_2} & \cdots & e^{j\omega_p} \\ \vdots & \vdots & \ddots & \vdots \\ e^{j\omega_1(M-1)} & e^{j\omega_2(M-1)} & \cdots & e^{j\omega_p(M-1)} \end{bmatrix} = \Theta \mathbf{T}^{-1} \quad (19)$$

and can be converted to the observability matrix  $\Theta$  of any other state-space realization via the appropriate regular state transformation  $\mathbf{T}$ . Noting that the rows of  $\Theta_d^H$  are formed by vectors  $\mathbf{z}^t(z = e^{j\omega_k})$  as in (9) and that at the signal frequencies  $G_f(z = e^{j\omega_k}) = 0$ , the relationships

$$\Theta_d^H \Gamma = (\mathbf{T}^{-1})^H \Theta^H \Gamma = \mathbf{0} \quad \text{and} \quad \Theta^H \Gamma = \mathbf{0} \tag{20}$$

immediately follow. Via (20) it can be shown that  $\Theta$  and  $\Gamma$  from which frequencies can be determined as described above are available from the data- or the data covariance matrix in a one-step procedure.

As shown in (21), the left singular vector matrix yielded by a singular value decomposition (SVD) of either  $\mathbf{S}$  or  $\mathbf{R}_{ss}$  can be partitioned after  $p$  columns into the desired matrices,

$$\mathbf{S} = [\Theta \mid \Gamma] \left[ \begin{array}{c|c} \Sigma_{S,1} & \mathbf{0} \\ \hline \mathbf{0} & \mathbf{0} \end{array} \right] \left[ \begin{array}{c} \mathbf{V}_{S,1}^H \\ \mathbf{V}_{S,2}^H \end{array} \right]$$

and

$$\mathbf{R}_{ss} = [\Theta \mid \Gamma] \left[ \begin{array}{c|c} \Sigma_{R,1} & \mathbf{0} \\ \hline \mathbf{0} & \mathbf{0} \end{array} \right] \left[ \begin{array}{c} \mathbf{U}_{R,1}^H \\ \mathbf{U}_{R,2}^H \end{array} \right] \tag{21}$$

Based on the common principles described, the model-based algorithms differ by either starting from the data- or the data-covariance matrix, applying different methods for reducing the effects of noise, and obtaining final frequency estimates in a more sophisticated way than the straightforward approach presented above.

To compare results of the model-based approach to those obtained from the FFT using the boxcar (FFTbp) as well as the Hanning window (FFTbp) and fit of a parabola, four algorithms—two polynomial- and two state-space-based—have been selected for this work. Indicated in the following list are briefly only the underlying principles, for additional information the reader is referred to the original publications:

- The Tufts and Kumaresan Variant of the Prony frequency estimation procedure (TKV): A linear system of equations derived directly from the linear predictability property (8), is solved for a single coefficient vector after computing a low-rank approximation to the unperturbed data by performing an SVD on the raw data matrix [8].
- Multiple Signal Classification (MUSIC): Starting from a factorization of the data covariance matrix, a polynomial with second-order

roots at the frequency locations on the unit circle is defined from a combination of all coefficient vectors obtained [9,10].

- Fast Estimation of Signal Parameters via Rotational Invariance Techniques (FESPRIT): A Karhunen–Loève Transform is applied to two data covariance matrices, frequencies are directly computed as a solution to a generalized eigenvalue problem [11].
- Toeplitz Approximation Method (TAM): A total-least-squares solution to (13) is computed from the partition of the left singular vector matrix of the data covariance matrix [6].

## 5. Model Order Estimation

A challenging problem in conjunction with model based evaluation is the correct estimation of the model order  $p$  [12]. The model order determines the dimension of the square state feedback matrix  $\mathbf{A}$  and corresponds to the number of sinusoidal components in the signal  $y_n$ . In the case of measurement data the model order is generally not known a priori, with the exception of applications where the number of targets is fixed by design, such as in surface acoustic wave (SAW) tag identification [13].

The nature of microwave distance sensor signals leads to a high number of superimposed response signals with different frequencies resulting from free space propagation with a multitude of objects and thus an unknown number of reflections within the radar path. Due to the geometrical extent of real targets, the point scatterer model (6), which is assumed by algorithms described above, is not exactly valid in reality, which leads to a blurring of individual target responses.

A deviation of the chosen model order from the correct number of sinusoidal signal components leads to incorrect results. Selecting the model order too low inevitably results in loss of signal components, and possible errors in the remaining targets. A model order higher than the optimum may result in large spurious peaks hiding the wanted signals. These artifacts can be used to adaptively determine the best model order for the problem on hand as will be shown later.

A model order prediction can be performed with the singular value spectrum of the data covariance matrix. In the noise-free case and when the data ideally match the model, there exist exactly  $p$  non-zero singular values in accordance with the model order  $p$ . In the practical case a noticeable gap between the  $p$  greatest singular values and the remaining smaller ones is expected, but on real data this gap nearly disappears, and reliability of this simple method is not sufficient.

Other statistical criteria like the Akaike Information Criterion (AIC) [14] or the Minimum Description Length criterion (MDL) [15,16]

also fail when applied to real sensor data with typical systematic distortions. A method for determining the number of sinusoids in white noise [7] performs slightly better on measurement data, but is still not reliable enough.

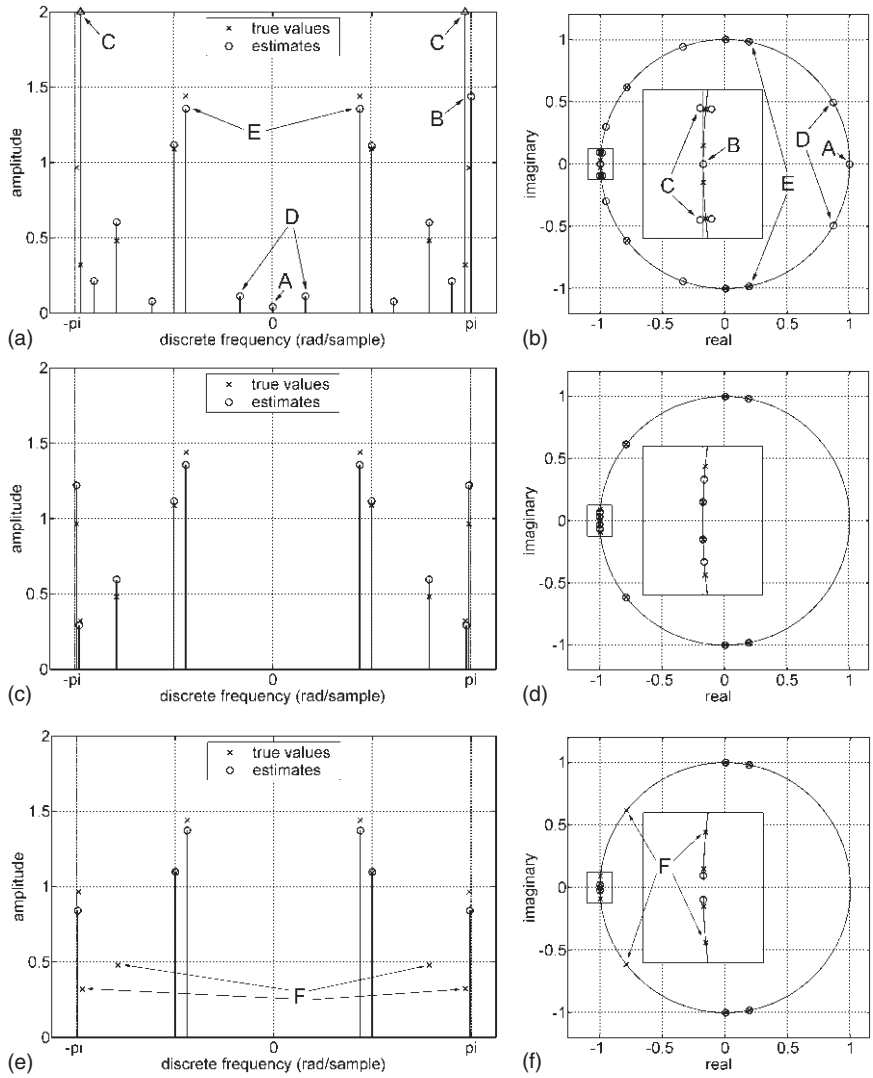
Best results were obtained with a completely different approach. In this adaptive method unwanted effects caused by a wrong model order are monitored and the model order is adapted to minimize spurious signals.

Figure 3 illustrates the unwanted effects caused by wrong model orders. The plots (a), (c), and (e) show the amplitudes versus frequency of the spectral components, whereas the plots (b), (d), and (f) depict eigenvalues of the state feedback matrix in the complex plane. The model used in this simulation is of order five with additive white Gaussian noise and a signal-to-noise ratio of 0 dB with respect to the average signal amplitude. True signal components are marked by “ $\times$ ”, estimates are marked by “ $\circ$ ”. An evaluation with the TAM algorithm and the correct model order, shown in Figure 3(c, d) yields results with high frequency accuracy. Amplitudes not estimated directly by the model based algorithm but in a second step, are of little interest in distance calculation. Figure 3(a, b) exemplarily shows effects that may occur if evaluation is performed with an incorrect model order of ten. Signal components with frequencies close to zero (A) or close to half the sampling rate (B) can erroneously appear. The spurious signals marked with (C) stem from two eigenvalues close together corresponding to complex frequencies, and exhibit extremely high amplitudes. Some signal components, e.g. (D), with small amplitudes additionally appear. Marker (E) shows a correctly identified signal component. The evaluation with a model order assumed too small is accompanied by a loss of information. This is shown in Figure 3(e, f) for a chosen model order of three and lost frequency components (F).

The adaptive algorithm starts with a quite high model order and the frequency estimates are observed with respect to the aforementioned effects. If one or more of them are encountered, the model order is reduced until a stable model order estimate without any spurious frequency components is obtained. Simulations and measurement results showed that this approach outperforms all statistical criteria mentioned above by far in FMCW signal evaluation.

## 6. Simulation of Resolution Enhancement

Too many parameters are involved to compare the abovementioned algorithms with a single measurement or by a simple statement. Therefore,



**Figure 3.** Evaluation results with an assumed model order (a), (b) higher than, (c), (d) equal to, and (e), (f) lower than the correct number of sinusoidal components. In the simulation an SNR of 0 dB with respect to the average signal amplitude was used. Diagrams (a), (c), and (e) show the calculated signal amplitudes vs. discrete frequency, whereas in (b), (d), and (f) the eigenvalues are plotted in the complex plane.

simulations under many different boundary conditions were carried out, and the results are compared in a statistical manner.

The main goal is to show the capability of resolving two closely located targets in an FMCW scenario, which corresponds to signal frequencies close together. As demonstrated in the FFT section, the signal phase has an important influence on the resolution capability. For the following simulations two signals with frequencies  $\omega_1$  and  $\omega_2$  are considered to be resolved if the estimated frequencies lie within a tolerance band of  $\pm|\omega_1 - \omega_2|/2$  around the true value and the amplitudes are within a window of  $\pm 50\%$  from the actual value. Every plotted point is averaged out of 100 simulations with  $N = 128$  data points each and random phase differences between the signal components.

The first simulation treats the detection probability of two signal components (targets), as defined before, with identical amplitudes as a function of SNR (varying from 0 to 40 dB) and frequency difference (varying from 0.005 to 0.1 rad/sample). Results for six different algorithms are plotted in Figure 4, namely (a) FFTbp, (b) FFThp, (c) TKV, (d) MUSIC, (e) FESPRIT, and (f) TAM. The FFT spectral grid spacing and hence the nominal resolution in that case corresponds to  $2\pi/128 = 0.049$  rad/sample. Especially for frequency differences below this value the results clearly show the limitations of both FFT variants (a, b) with respect to resolution capability. Due to the narrower main lobe, the boxcar window produces better results than the Hanning window, as far as only resolution is considered (see also Figure 8). At the nominal FFT resolution limit all model-based algorithms exhibit noticeably better results (c–f). The FFT is insensitive against SNR degradation, but its performance is clearly limited by the frequency difference. TKV, MUSIC, and TAM show similar results with a dependence on SNR and  $\Delta\omega$ , whereas the FESPRIT also saturates for very small frequency differences essentially independent of the SNR. For better comparability results at an SNR of 20 dB are additionally marked with a thick solid line in Figure 4 and plotted in Figure 9(b).

In the second simulation the SNR remains constant at 20 dB with respect to the target of fixed frequency and amplitude. Instead of varying the SNR, the amplitude of the smaller signal component changes from a signal power ratio compared to a fixed target of 0 to 40 dB. The frequency differences are the same as before. Figure 5 shows the simulation results of the detection probability for the six different algorithms. The leakage of the main peak in the FFT evaluation, especially when the boxcar window is used, very quickly masks smaller signal components as their amplitude decreases. The wider main lobe of the Hanning window as compared to the boxcar window, however, more quickly leads to overlapping, which results in an overall lower resolution capability. All model-based algorithms exhibit a similar behavior

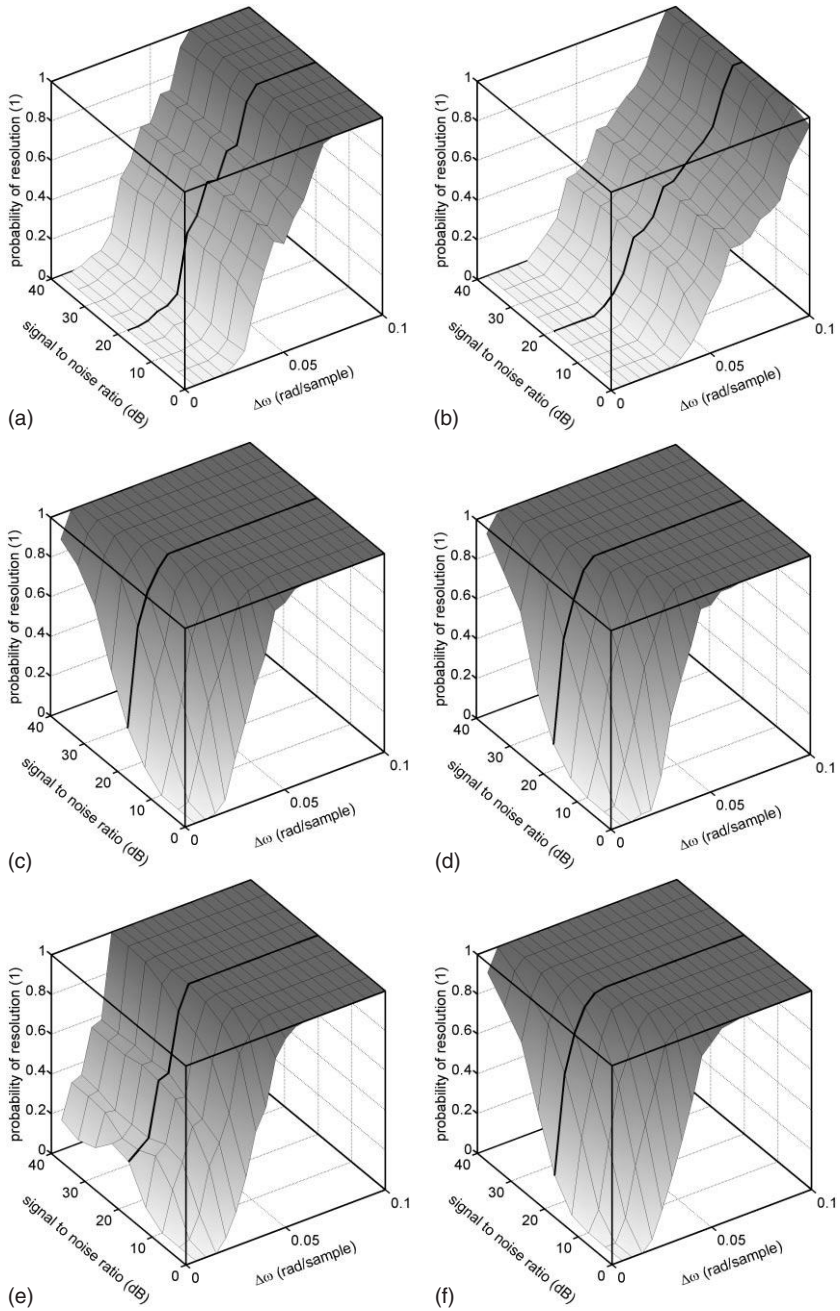


**Figure 4.** Detection probability of two targets with identical amplitudes as a function of SNR and frequency difference for different algorithms (a) FFTbp, (b) FFThp, (c) TKV, (d) MUSIC, (e) FESPRIT, and (f) TAM.

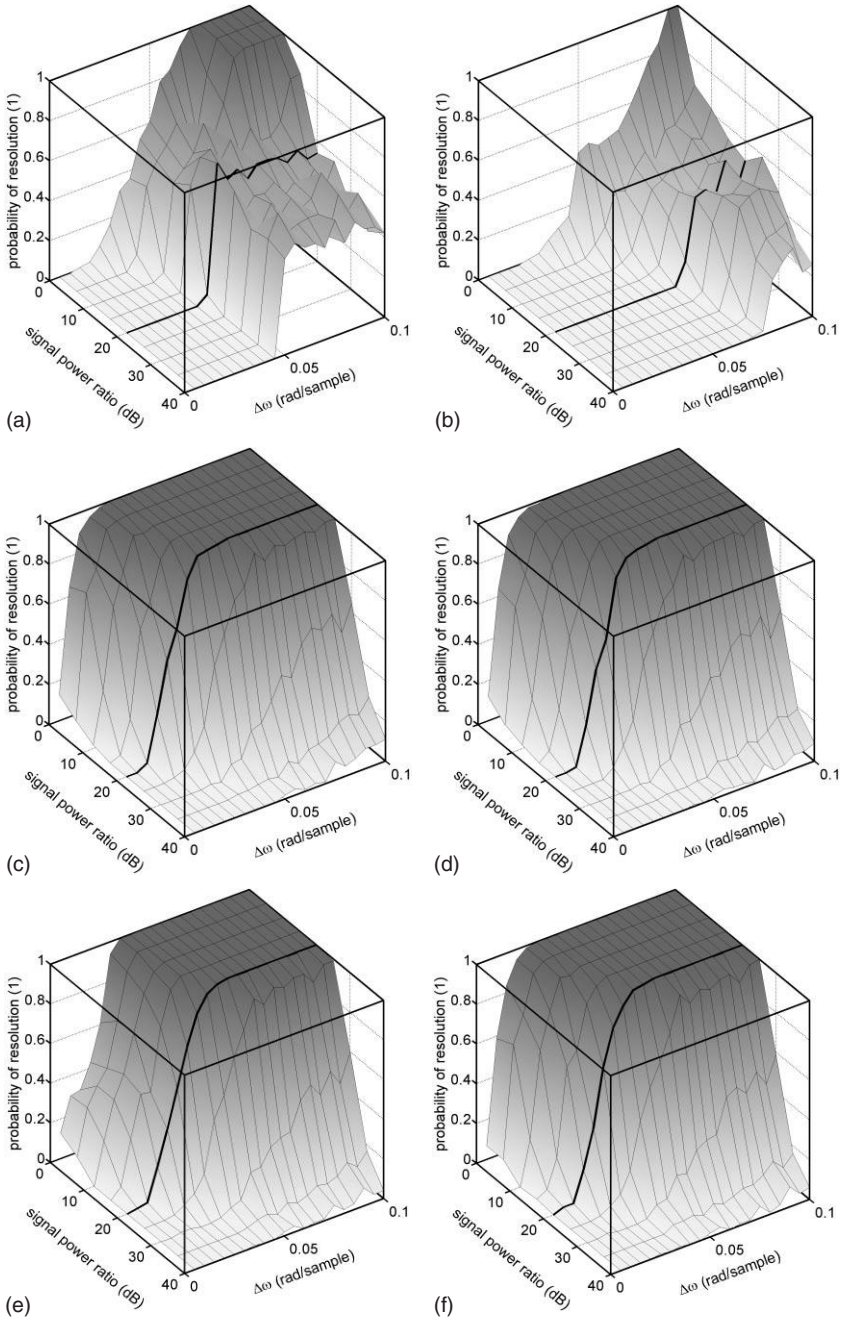


**Figure 5.** Detection probability of two targets with an SNR of 20 dB as a function of signal power ratio and frequency difference for different algorithms (a) FFTbp, (b) FFThp, (c) TKV, (d) MUSIC, (e) FESPRIT, and (f) TAM.

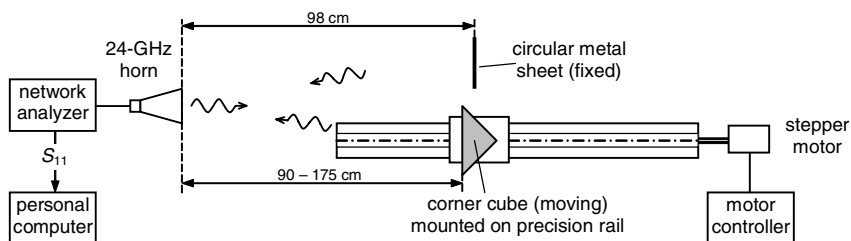


Figure 6. Schematic of the test measurement setup.

with a degradation in resolution ability first at a power ratio of 25 dB. The curves in Figure 5 at a signal power ratio of 20 dB are highlighted for better readability.

## 7. Measurement Setup

To verify simulation results and to analyze the behavior of the different algorithms when applied to real radar signals a test setup as shown in Figure 6 was used. Measurements were taken with a vector network analyzer around 24 GHz with two targets under laboratory conditions, but not in an anechoic chamber. Therefore, some background echoes and multipath responses can be found in the measurement data. The fixed target was a circular metal sheet and the moving target was a corner cube, with reflection coefficients for both targets being in the same order of magnitude.

Starting at 22 GHz, 801 frequency points equally spaced 5 MHz apart were taken at each individual arrangement with the moving reflector starting about 10 cm closer to the horn and moving away 1 cm every measurement cycle. The fixed target was located at a distance of 98 cm from the front of the horn antenna.

## 8. Measurement Results

The raw data cover a bandwidth of 4 GHz with a center frequency of 24 GHz. As stated in Eq. (5) the initial phase depends not only on the target distance, but also on the sweep starting frequency. Therefore, to get a statistical distribution over different phase angles, data vectors with 256 data points each, shifted by two data points for each evaluation, are taken out of the raw data so that 273 individual results per target position are available. Due to the limited frequency range of the horn antenna the obtained initial phase difference between reflections from fixed and moved target does not cover a range of  $2\pi$  below a distance difference of 5.5 cm, but gives enough points to show the general behavior. With  $N = 256$  samples and a frequency step of 5 MHz the corresponding Fourier resolution in distance is 11.7 cm.

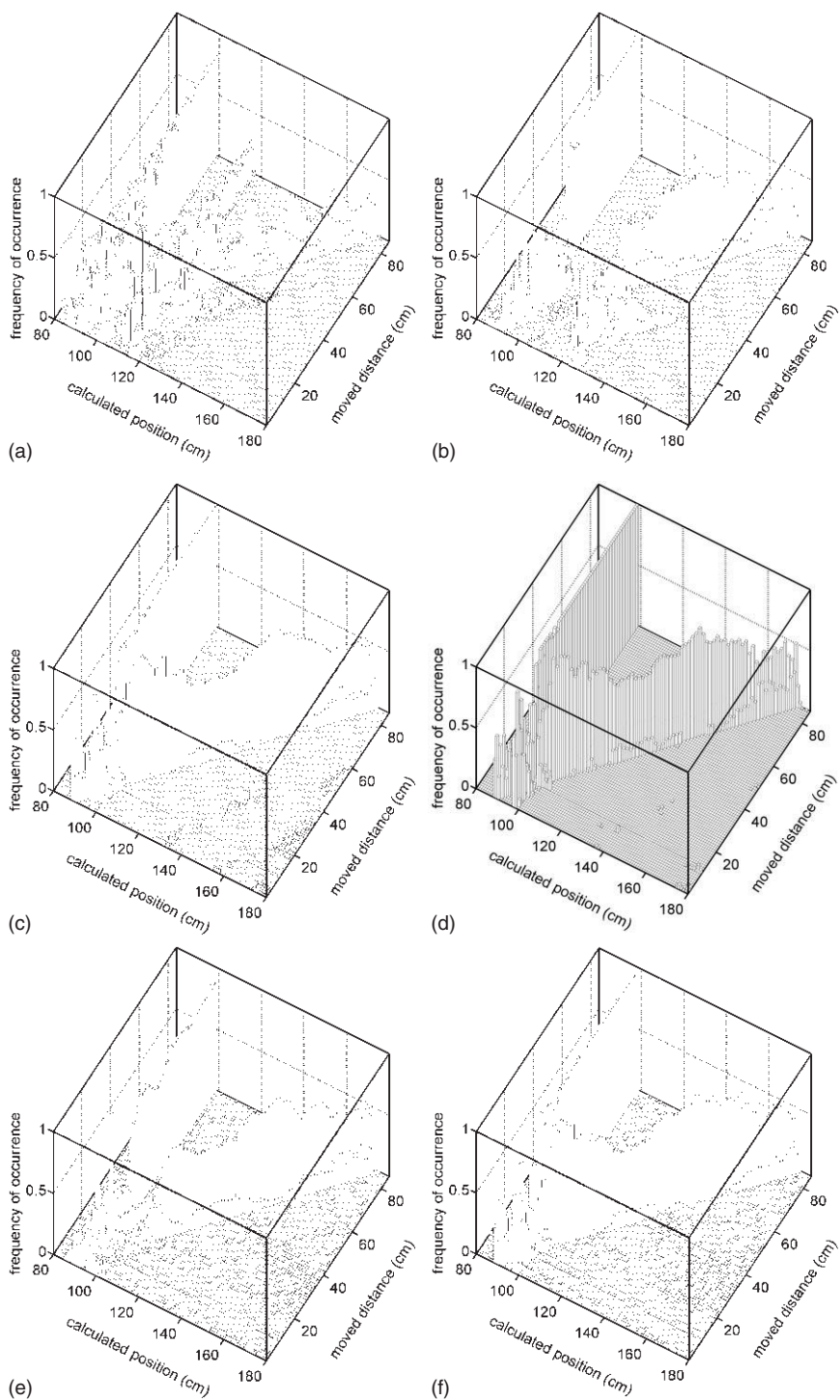
Apart from the radar echoes originating from the two reflectors, the simple test setup creates several unwanted reflections that appear as additional targets such as the wall in the background, the discontinuity at the coaxial connector, the coaxial to waveguide transition, and multipath reflections.

Figure 7 shows the summarized evaluation results, plotted as frequency of occurrence of the respective distance estimate (in cm) for every position the target was moved to (in cm) for a center frequency of 24 GHz, a bandwidth of 1280 MHz,  $N = 256$  samples, and 273 measurements at each position. The model order in the test setup was  $p = 6$  signal components, covering the two distinct targets and additional reflections at the antenna and from the background.

The frequency estimates corresponding to the fixed and moved targets are clearly recognizable in all plots—as long as the difference in target distance is high enough. In the lines the estimates form, the region around 10 cm of moved distance, where both targets are at similar absolute distances to the antenna, is especially noteworthy. The model-based algorithms, especially the TKV, MUSIC and TAM algorithms deliver two separate bars even for very small frequency differences, while for the FFT-based algorithms, two bars merge into one, long before the intersection is reached. What can also be seen in the FFTbp plot is that even when the two targets are resolved, the relatively high sidelobes of the spectrum of the boxcar function exceed other signal components in many cases and bring about an unwanted row of bars parallel to that corresponding to the main peak.

Depicted in Figure 8 is the standard deviation of the distance estimate for the fixed target over the distance to the moved target as derived from measurements. For very low frequency differences the standard deviation increases from zero at equal distance to considerably high values of several centimeters. As already expected from the illustrations in the FFT-section, a close-by disturbing target obviously degrades the precision of frequency estimates considerably, especially for the FFT-based frequency estimators. Also, though with the Hanning-window the standard deviation reaches a higher global maximum value, it declines relatively rapidly to values comparable to most model-based algorithms. With the boxcar-window, in contrast, it finally approaches a higher value only after attaining several further maxima.

Comparing Figure 9(a) that shows the results from resolution evaluation for algorithms applied to measured data to Figure 9(b) that contains simulation results for a signal to noise ratio of 20 dB proves very good agreement between resolution probability derived from simulated and measured data. Note that a target distance difference of 10 cm in Figure 9 is



**Figure 7.** Frequency of occurrence of distance estimates as a function of real movement with 256 samples spaced 5 MHz apart and a center frequency of 24 GHz for different algorithms (a) FFTbp, (b) FFThp, (c) TKV, (d) MUSIC, (e) FESPRIT, and (f) TAM.

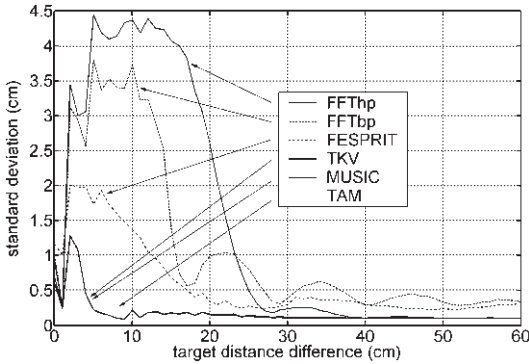


Figure 8. Standard deviation of the position estimate for the fixed reflector as a function of the distance difference between reflectors with respect to the antenna.

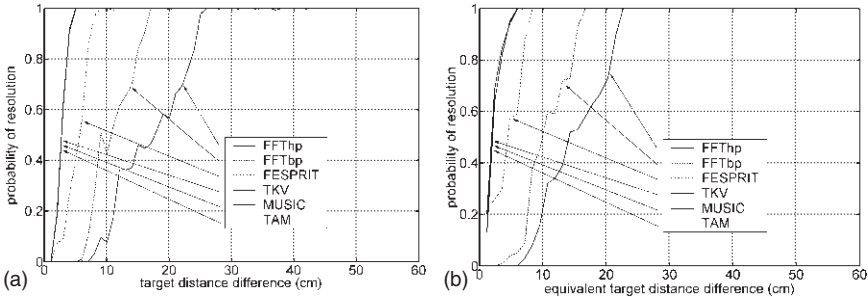


Figure 9. Detection probability of two targets as a function of the distance difference between reflectors with respect to the antenna. Shown in (a) are results from measurements and in (b) from simulated data taken from Figure 4.

equivalent to a discrete frequency of 0.042 rad/sample in Figure 4. Clearly, as concluded before from simulations, model-based frequency estimation delivers a significantly lower resolution limit.

### 9. Conclusion

With the application of state-of-the-art frequency estimation algorithms to the evaluation of linear FMCW/FSCW distance radar measurement data, a much better resolution capability for closely spaced targets, and an enhancement in distance accuracy can be achieved. The general resolution problem was sketched on the FFT spectrum and then simulations for closely spaced targets under different constraints and using different algorithms

were performed, and the results were viewed in a statistical manner. Consequences of incorrectly estimated model orders used in the evaluation process were pointed out and the model order estimation problem was treated by an adaptive model order selection procedure yielding reliable estimates with measured radar sensor data. Measurements with a fixed and a moving target were carried out to confirm simulation results. The results correspond very well to those of the simulations and confirm the improvement in resolution and accuracy with model-based frequency estimation algorithms as compared to the FFT. These advantages must be paid for with higher computational cost and an extra task for the determination of the model order in general applications. Progress in digital signal processing hardware makes this approach very promising for radar sensors in industrial applications such as distance sensors in the steel industry or for liquid level sensors [17].

## References

1. Cooley, J.W. and Tukey, J.W., 1965, An algorithm for the machine computation of the complex fourier series: *Mathematics of Computation*, v. 19, no. 4, p. 297–301.
2. Pichler, M., Stelzer, A., Kolmhofer, E., and Weigel, R., 2001, Velocity estimation from Doppler radar measurements: *Proc. of Int. Symp. Theoret. Elec. Eng., ISTET-2001, Linz, Austria*, v. 2, p. 369–374.
3. Stelzer, A., Pichler, M., and Weigel, R., 2002, High resolution algorithms applied to velocity and length-of-travel measurements in radar sensors: *Proc. of Asia Pacific Microwave Conf., APMC-2002, Kyoto, Japan*, v. 1, p. 245–248.
4. Proakis, J.G. and Manolakis, D.G., 1996, *Digital signal processing: Principles, algorithms, and applications*, 3rd ed., Prentice Hall, Upper Saddle River, NJ, USA.
5. Kay, S.M., 1988, *Modern spectral estimation: Theory and application*, Prentice Hall, Englewood Cliffs, NJ, USA.
6. Rao, B.D. and Arun, K.S., 1992, Model based processing of signals: A state space approach: *Proc. of IEEE*, v. 80, no. 2, p. 283–309.
7. Fuchs, J.J., 1988, Estimating the number of sinusoids in additive white noise: *IEEE Trans. on Acoustics, Speech and Signal Processing*, v. 36, no. 12, p. 1846–1853.
8. Tufts, D.W. and Kumaresan, R., 1982, Estimation of frequencies of multiple sinusoids: Making linear prediction perform like maximum likelihood: *Proc. of IEEE*, v. 70, no. 9, p. 975–989.
9. Rao, B.D. and Hari, K.V.S., 1989, Performance analysis of Root-MUSIC: *IEEE Trans. on Acoustics, Speech and Signal Processing*, v. 37, no. 12, p. 1939–1949.
10. Stoica, P. and Nehorai, A., 1989, MUSIC, maximum likelihood, and Cramer–Rao bound: *IEEE Trans. on Acoustics, Speech and Signal Processing*, v. 37, no. 5, p. 720–741.
11. Yuan Hwang, C. and Chao Hung, C., 1992, An alternative algorithm based on subspace rotation invariance techniques for directions-of-arrival estimation using the compressed data pencil: *J. Acoustical Soc. of Am.*, v. 92, no. 4, pt. 1, p. 1962–1965.
12. Gulden, P., Vossiek, M., Storck, E., and Heide, P., 2001, Application of state space frequency estimation techniques to radar systems: *Proc. of 2001 IEEE Int. Conf. Acoustics, Speech, and Signal Processing*, Salt Lake City, UT, USA, v. 5, p. 2870–2880.

13. Pichler, M., Stelzer, A., Schuster, S., Scheibhofer, S., and Hauser, R., 2003, High resolution evaluation algorithms for SAW-identification tags: Proc. of Modeling, Signal Processing, and Control Conf. at SPIE's 10th Smart Structures and Materials Symp., San Diego, CA, USA, (in print).
14. Akaike, H., 1971, Information theory and an extension of the maximum likelihood principle, Proc. of 2nd Int. Symp. Inform. Theory—Abs. of Papers, Tsahkadsor, Armenia, USSR, p. 276–281.
15. Wax, M. and Kailath, T., 1985, Detection of signals by information theoretic criteria: IEEE Trans. on Acoustics, Speech and Signal Processing, v. ASSP-33, no. 2, p. 387–392.
16. Zhao, L.C., Krishnaiah, P.R., and Bai, Z.D., 1987, Remarks on certain criteria for detection of number of signals: IEEE Trans. on Acoustics, Speech and Signal Processing, v. ASSP-35, no. 2, p. 129–132.
17. Pichler, M., Gulden, P., Vossiek, M., and Stelzer, A., 2003, A 24-GHz tank level gauging system with state-space frequency estimation and a novel adaptive model order selection algorithm: Proc. of 2003 IEEE MTT-S Int. Microwave Symp., Philadelphia, PA, USA.

# Enhanced Auditory Displays for Discriminating Landmines from Clutter Using Electromagnetic Induction Sensors

Yingyi Tan, Lisa G. Huettel, Stacy L. Tantum, and Leslie M. Collins\*

Department of Electrical and Computer Engineering, Box 90291,  
Duke University, Durham, NC, USA

*Received June 13, 2002; revised February 18, 2003*

---

Landmine detection is primarily performed using electromagnetic induction (EMI) sensors. These sensors detect the presence of metal and convey the information to the sensor operators via an audio signal. Reduction of false alarms from objects that contain metal but are not landmines, i.e. discrimination, is a challenging problem. Recent work on automated algorithms has shown promise towards reducing false alarm rates of EMI sensors. In this study, the audio signal was modified to encode the presence of metal as well as information regarding mine/non-mine belief in order to determine whether the additional information enabled operators to better discriminate mines from clutter. Using data collected from real landmines, we experimentally investigated which perceptual dimensions most effectively convey different aspects of the information contained in the sensor response to a listener. Results indicated that the presence of metal (detection) could be coded in the fundamental frequency of the audio signal, and that mine/non-mine belief (discrimination), determined using an automated algorithm, could be coded in a separate audio dimension. Operators performed better with this audio coding scheme than one where only metal content information was presented via the fundamental frequency of the audio signal.

---

**Key Words.** Auditory display, Bayesian signal processing, landmine detection, discrimination, electromagnetic induction.

## 1. Introduction

Landmines are a form of unexploded ordnance, usually emplaced on or just under the ground. They are designed to explode in the presence

---

\*To whom all correspondence should be addressed. Phone: 919-660-5260; fax: 919-660-5293; e-mail: lcollins@ee.duke.edu

of a triggering stimulus such as pressure from a foot or a vehicle. Generally, landmines are divided into two categories: antipersonnel mines and anti-tank mines. Antipersonnel (AP) landmines are typically devices designed to be triggered by a relatively small amount of pressure, typically 40 lbs. AP mines contain a small amount of explosive so that the explosion of the landmine maims or kills the person who triggers the device. In contrast, antitank (AT) mines are specifically designed for the destruction of tanks and vehicles. Pressure-activated AT mines explode only if compressed by an object weighing hundreds of pounds. AP mines are generally small (less than 10 cm in diameter), and are usually more difficult to detect than the larger AT mines.

According to several sources (including the United Nations, the U.S. State Department, the Red Cross, and various humanitarian agencies), it is estimated that there are over 100 million landmines buried across 70 countries, with an estimated 2 million more emplaced each year. Fewer than 100,000 landmines are reportedly cleared each year, and estimates indicate that landmines kill or maim at least 26,000 people annually. Most victims are innocent civilians, many of whom are children. Once laid, mines can maim or kill for decades after all hostilities have ceased. For this reason, the antipersonnel landmine has been referred to as a “weapon of mass destruction in slow motion” [1].

Mine detection technologies and systems that are in use or have been proposed for use include electromagnetic induction (EMI), ground penetrating radar (GPR), infrared imaging (IR), and quadrupole resonance (QR). Regardless of the technology applied to the problem, the goal is to achieve a high probability of detection ( $P_d$ ) while maintaining a low probability of false alarm ( $P_{fa}$ ). This is of particular importance for the landmine problem since the nearly perfect  $P_d$  that is necessary to comply with safety requirements comes at the expense of a high  $P_{fa}$ , and the time and cost required to remediate contaminated areas are directly proportional to  $P_{fa}$ . In areas such as a former battlefield, the average ratio of real mines to suspect objects is 1:100, thus the process of clearing the area proceeds very slowly.

Among the technologies available for landmine detection, the most well-established is the EMI sensor, or metal detector. EMI sensors transmit a primary electromagnetic field that induces currents in any metallic or conducting object in the surrounding medium. These eddy currents in the metallic object produce a secondary electromagnetic field that can be measured by the sensor. The measured signal can be modeled as a weighted sum of decaying exponential signals in the time domain, or as a weighted sum of the Fourier transform of decaying exponential signals in the frequency domain [2–12]. Since the decay rates are inherent properties of a particular object and are not dependent on target/sensor orientation [12], decay rate estimation

has been proposed as a robust approach to the problem of discriminating landmines from clutter [2–7]. This approach can be applied to both time and frequency domain EMI data.

Recently, substantial research efforts have been focused on optimizing the signal processing performed by the analysis portion of the landmine detection system. Previous work directed toward developing algorithms for both time- and frequency-domain EMI systems has shown that the false alarm rate can be reduced dramatically by improving the signal processing [2–15]. It has also been established that the human operator, usually a soldier in military demining scenarios, is a key component in the overall mine detection system. Recent research on the effects of training [16–17] has shown that operator training can have a substantial impact on performance, with well-trained operators dramatically outperforming poorly trained or untrained operators. This result holds both for single sensor systems and for multi-sensor suites. Unfortunately, most operators are not adequately trained on the currently deployed technology, although this is slowly changing.

In currently deployed systems, human operators (both soldiers and civilians) are often plagued by extremely high false alarm rates as a result of the extensive amount of metallic clutter in the environment. In addition to a lack of training, inadequate or incomplete presentation of the sensor information to the operator may also cause poor performance. Not only is a very limited amount of the information in the sensor response provided to the operator, but the manner in which the information is presented, the audio signal coding, may not fully utilize the operator's auditory processing abilities. Unluckily, it is difficult to assess the relative contributions of the sensor and the sensor operator in a field scenario. Thus, theoretical and experimental studies of algorithm performance on data collected in field exercises are often undertaken to allow *potential* improvements due to signal processing to be assessed independently of the sensor operator. Independent studies that assess performance of the combined system (hardware, algorithm and operator) in the field are routinely performed as part of government-sponsored prove outs.

The literature regarding the design of alarm or auditory warning signals suggests that pulsed signals consisting of harmonic complexes effectively convey information [18–20]. This literature also reports that information is most efficiently transmitted via frequency as opposed to amplitude cues, and that urgency can be effectively transmitted in audio signals via changes in pulse rate. This literature has not been exploited when designing alarm signals for landmine detection systems, and proposed changes based on this literature have not been tested in human subjects [20]. Rather, the current practice is to reduce the system response to a single value, or metric, based

only on the strength of the signal, and to convey this metric through an increase in the frequency of a narrow band, continuous signal. The metrics currently used in fielded time domain EMI systems consist of a single time sample of the signal, a sum of the signal over a particular time window, or the energy in the signal. Each of these metrics increases as the amount of metal present increases, and decreases as the distance between the detector and the object increases. By themselves, these metrics do little to discriminate between metallic clutter items and landmines.

The goal of the current study was to combine an investigation of the performance of signal processing algorithms for improved false alarm rate performance with an investigation of the performance of a human listener when multiple lines of information are being presented. Specifically, we investigate methods by which such EMI signal processing algorithms could be integrated with audio signal generation techniques in order to better utilize the audio processing capabilities of the human operator. We present the results of a study that investigates the perceptual dimensions that were the most effective in transmitting the information contained in an EMI signal to naïve, or un-trained, listeners. We were specifically interested in whether information regarding metal content could be conveyed in one audio dimension while landmine confidence could be simultaneously conveyed in a second audio dimension. Current approaches convey only information regarding metal content, as modified by distance, in a single-dimensional signal. Specifically, such current approaches are limited to the *detection* problem, in which the presence of metal is determined using the EMI system. We are interested in pursuing the *discrimination* problem, where landmines are differentiated from other metal objects. Our goal is to provide information regarding both the detection and discrimination problem to the operator and determine whether they can use such information effectively. We also investigated the degree to which improvements in performance measured for automated signal processing algorithms could be translated into improvements in performance for an operator. A set of data collected with a deployed EMI sensor over real landmines buried at a government test site was used to analyze performance improvements.

## 2. EMI Sensor Model and Field Data

Most currently deployed EMI sensors are operated in the time domain. The frequency content of the transmitted pulse is usually fairly low (<1 MHz), a regime in which conductivity- and permeability-dependent skin depth of the materials varies significantly [3,21–24]. Also, the displacement current component of the response to the near field loop-induced fields is weak enough to be neglected [21–24]. It has been shown [3,5,21,24] that the

response,  $r(t)$ , measured by a pulsed EMI system from a general conducting, permeable target can be modeled as a superposition of weighted, resonant responses:

$$r(t) = \sum_{i=1}^n A_i e^{j\omega_i t}$$

where  $\omega_i$  is the  $i$ th natural resonant frequency of the object and  $A_i$  is the initial magnitude of the response corresponding to the  $i$ th frequency. In practice, the real part of  $\omega_i$  is very small and can be neglected [21,24]. Thus, the response measured by a pulsed EMI system can be accurately modeled as a weighted sum of exponential modes:

$$r(t) = \sum_{i=1}^n A_i e^{-\alpha_i t}$$

The magnitudes of the excited modes,  $A_i$ , depend strongly on the excitation level, depth, and orientation of the subsurface object. The decay rates,  $\alpha_i$ , are a function of object size, shape, conductivity and permeability, which are hopefully unique to each landmine type. While several studies have suggested that the decay rates from each type of landmine form distinct sets [2–5], there is no evidence that clutter will not share the same decay rates space as landmines. Previous discrimination work has suggested that while overlap between the sets of decay rates occurs between mines and metallic clutter, the overlap is not complete [2–15]. The number of decay rates that can be accurately estimated from a measured signal depends on the signal-to-noise ratio (SNR) of the signal. This limit has been quantified for EMI sensors by calculation of Cramer–Rao lower bounds [25,26].

There are two general classes of time-domain EMI sensors: single channel, also called integrated time-domain systems, and multi-channel time-domain systems. A single channel sensor, which constitutes the conventional EMI sensor, performs an operation (either selection of a single sample in time, calculation of the sum over a set of samples, or calculation of the energy) on the measured time-domain response over a predetermined signal window to obtain a scalar value at each location interrogated by the sensor. In contrast, a multi-channel sensor records a set of sampled values of the response waveform at each interrogated location.

For this study, we utilized data collected with the standard Army landmine detector, the PSS-12, which is manufactured by Schiebel Corporation. In its fielded operation mode, which is designed to locate all subsurface metallic anomalies, the internal circuitry of this EMI sensor controls the transmit pulse and gates the received signal, which is sampled a preset amount of time after the signal falls out of saturation. An estimated background

signal is subtracted from this sampled value and this difference is compared to a threshold set by the operator. The resulting signal is used to drive a voltage-to-frequency converter to generate an audio tone. The operator then interprets this tone to determine whether a metallic object is present (detection). In order to collect higher-information content data with this sensor, the PSS-12 has been modified so that the entire signal obtained at the receive coil could be measured [27]. The measured response was captured automatically from the receive coil via custom-designed software written in LabVIEW™. An example of the signal measured from a landmine using the modified PSS-12 is shown with the solid line in Figure 1. The sensor output is plotted as a function of time and the characteristic form of a decaying exponential signal can be clearly observed.

The Joint UXO Coordination Office (JUXOCO), located at Fort Belvoir, VA, has developed a Performance Baseline and Test Site designed

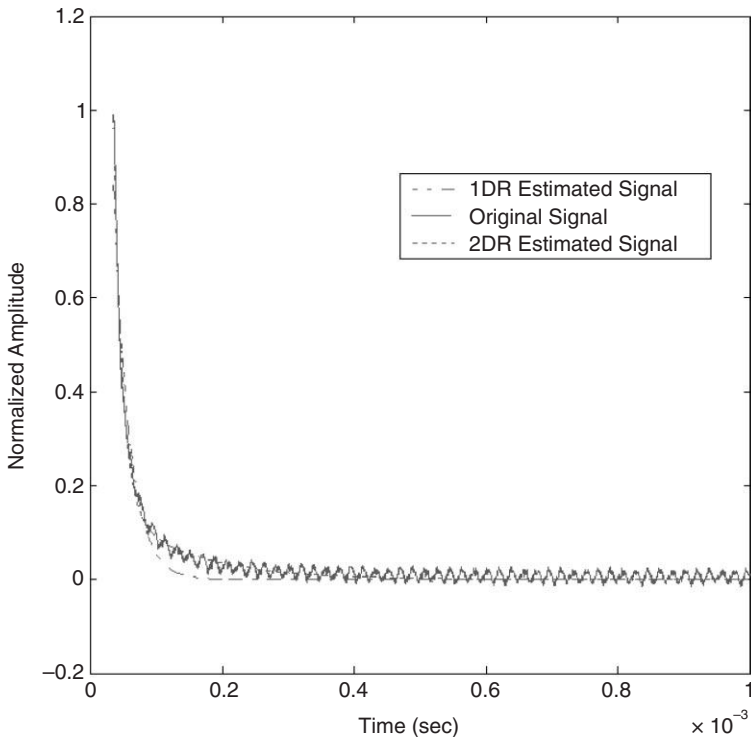


**Figure 1.** Response from a landmine measured with the PSS-12 as a function of time (solid line) and predicted signature showing a fit using one decay rate (dashed line) and two decay rates (dotted line).

to evaluate the performance of handheld and vehicular landmine and unexploded ordnance (UXO) detection systems [28,29]. This site contains a 5 meter by 25 meter calibration area where both mines and anthropic clutter have been emplaced in the center of 1 meter by 1 meter grid squares. Each of the 125 grid squares has either nothing, a non-landmine object (clutter), or a landmine buried at the center, thus allowing discrete opportunities for detections and false alarms. All indigenous clutter has been removed from the site. The mine targets that have been emplaced in the grid squares are predominately low-metal content landmines since these provide the greatest challenge to currently fielded EMI sensors. Data were collected from the modified PSS-12 sensor at the center of each grid square in the calibration grid at the JUXOCO test site by researchers from Auburn University. A complete calibration lane data set was collected on three different days, resulting in three data sets reflective of slightly different environmental conditions. The collected signals were sampled at 20 MHz and saved to disk for further analysis.

### 3. EMI Signal Processing and Performance Analysis

In physics-based statistical signal processing, a phenomenological model describing the nature of the underlying signal is utilized within the framework of statistical decision theory. Tying the signal processing to the phenomenology, while continuing to acknowledge the statistical nature of the decision problem, often results in substantial performance gains. For the time domain EMI-based landmine scenario, the phenomenological model predicts that the signal measured at the receive coil is a weighted sum of decaying exponential signals. Since the decay rates are defining characteristics of the signal, a physics-based approach suggests extracting the decay rates and using them within the context of a statistical processor to make a mine/no-mine decision. Previous work has indicated that processing the entire signal, as opposed to processing the decay rates, provides better performance [7], however such algorithms can often not be implemented in real time. Because of the nature of the landmine problem, only real-time processing was considered to be viable in this study. Numerous techniques have been proposed previously for decay rate estimation. A novel method, nonlinear least squares estimation of the signal poles, provides better overall performance than other frequently used methods, such as nonlinear least squares estimation of the decay rates [25,30]. Instead of estimating the signal decay rates directly, nonlinear least squares estimation of the signal poles reparameterizes the underlying signal so that a function of the decay rates is first estimated, and then the decay rates are calculated from the intermediate estimates. Assuming for a moment that a single exponential is present, the

response of the EMI sensor may be written as

$$x(t) = Ap^{t/T_0}$$

where  $p = e^{-\alpha T_0}$  is referred to as a signal pole; and  $T_0$  is used to scale the poles in order to avoid numerical artifacts [30]. To minimize the error function, the sum of the squared differences between the modeled signal  $x(t)$  and the data  $r(t)$  measured by the EMI sensor,  $e = \sum (x(t) - r(t))^2$  is used to estimate the pole  $\hat{p}$ . The signal decay rate is obtained by

$$\hat{\alpha} = \frac{-\ln(\hat{p})}{T_0}$$

If the recorded signal consists of a weighted sum of multiple decay rates a similar approach can be utilized. Amplitudes associated with each of the decay rates are also estimated simultaneously using this method.

Numerical gradient searches were implemented to find the estimate of the pole. Ten sets of initial values for the amplitudes and the poles were used in order to overcome a limitation of numerical gradient searches: they are not guaranteed to find the global minimum of the error function. The decay rate that results in the minimum error between the estimated signal and the measured signal is then chosen as the estimate.

The signal-to-noise ratio present in the PSS-12 data allows a maximum of two decay rates to be reliably estimated [27]. We developed two processors, one that utilized a single estimated decay rate and one that utilized two estimated decay rates. Although the second of the two processors provides a more accurate fit to the experimental data, the first requires less computation time to perform the decay rate estimation. Figure 1 shows a comparison between the signal measured from a mine with the PSS-12 sensor and the signal generated using a fit from a single estimated decay rate (dashed line) and a fit using two estimated decay rates (dotted line). Clearly, in this case, the measured signal is better predicted when two decaying exponential functions are used to model the measured signal.

The statistical processor using a single decay rate is formed using the likelihood ratio test [31] and the test statistic,  $\Lambda$ , is given by

$$\Lambda(\hat{\alpha}) = \frac{p(\hat{\alpha}/H_1)}{p(\hat{\alpha}/H_0)}$$

where  $p$  denotes probability density function (pdf),  $\hat{\alpha}$  is a single estimated decay rate, and  $H_1$  and  $H_0$  are the mine and clutter (or no-mine) hypotheses respectively. It is important to note that this formulation is for the discrimination, as opposed to simply detection, problem since  $H_0$  includes both metallic clutter and bare ground. We will refer to this processor as the IDR processor. The pdfs that describe the decay rates under each hypothesis were

not known a priori and were estimated from the observations of the estimated decay rates from the measured real data. The estimated pdfs do not obey any commonly used unimodal pdf, thus the equation for the pdf that was adopted utilized a 20th degree polynomial fit to the measured distributions. Although the pdf derived using a polynomial fitting method provides a good fit to the data, we were concerned that it might be less robust than a mixed Gaussian pdf that superimposes several weighted-Gaussian pdfs, each with different means and covariance functions. However, the performance achieved using the two different pdf models was similar.

In the data, there were several cases where a single decaying exponential did not provide a good fit to the measured data, as illustrated in Figure 1. The decay rate processor was subsequently modified to process two estimated decay rates

$$\Lambda(\hat{\alpha}_1, \hat{\alpha}_2) = \frac{p(\hat{\alpha}_1, \hat{\alpha}_2/H_1)}{p(\hat{\alpha}_1, \hat{\alpha}_2/H_0)}$$

and this processor is denoted the 2DR processor. This processor is also designed for the discrimination problem.

The two decay rates extracted based on the algorithm described previously are not independent, thus the joint pdf must be estimated. Figure 2 illustrates the relationship between the two decay rates estimated from the PSS-12 data set collected at the JUXOCO site. Each symbol is associated with a particular decay rate pair that was estimated from the data set. As illustrated in Figure 2, the decay-rate pairs are not randomly scattered over the entire space; they are divided amongst several clusters, each with its own correlation structure. Assuming that each cluster follows a two-dimensional Gaussian distribution, then a Gaussian mixture model can be employed, i.e.,

$$p(\hat{\alpha}_1, \hat{\alpha}_2) = \sum_{i=1}^n w_i p_i(\hat{\alpha}_1, \hat{\alpha}_2)$$

where the  $i$ th pdf,  $p_i$ , is a Gaussian pdf:  $N(\boldsymbol{\mu}_1, \boldsymbol{\mu}_2, \boldsymbol{\sigma}_1^2, \boldsymbol{\sigma}_2^2, \boldsymbol{\rho})$  and  $w_i$  is the weighting coefficient associated with the  $i$ th cluster. The means, variances, and correlation coefficient can be estimated for each cluster from the data. The weights are defined as the proportion of mines in each cluster relative to the total number of data points.

One important issue in determining the pdfs under each hypothesis is finding a robust means by which to group the data into the clusters that define the parameters of the individual Gaussian pdfs. A simple approach is to simply group, or cluster, the decay rates manually. In this brute force approach, the number of clusters is determined by visually inspecting a scatter plot of the decay rates. Each pair of decay rates is then assigned to

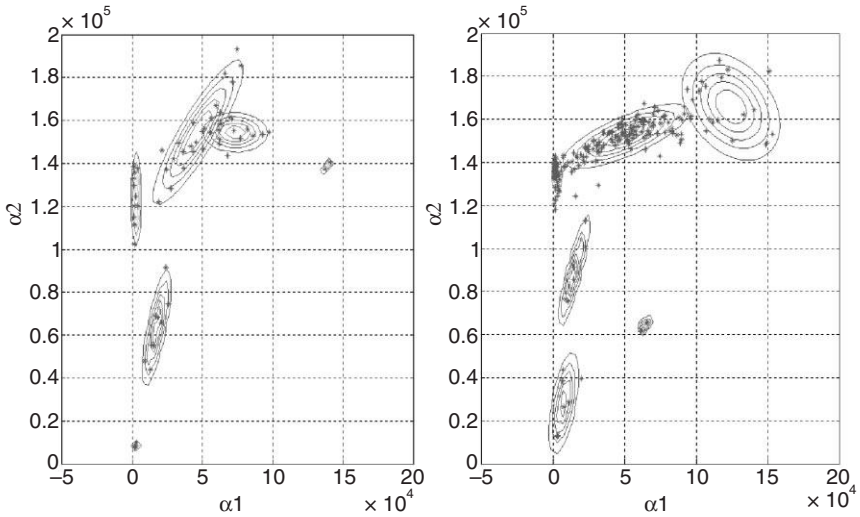


**Figure 2.** Scatter and contour plots showing the relationship between the two estimated decay rates,  $\hat{\alpha}_1$  and  $\hat{\alpha}_2$ , under the two hypotheses. The left hand plots contains data from mines ( $H_1$ ) and the right hand plots contains data from clutter objects. The symbols indicate an estimated decay rate pair, the solid lines indicate contour plots for 2-dimensional Gaussian functions fit to each cluster. Contours in the left panel were generated using brute-force clustering, and contours in the right panel were generated using the FCM clustering algorithm.

one of the clusters. Once the clusters have been defined, the mean and covariance function that defines the Gaussian pdf can be estimated from the data forming each cluster. Although this approach to clustering is valid, it is time consuming, thus automated approaches were also considered.

In fuzzy logic research, fuzzy c-means (FCM) is a data clustering technique wherein each data point belongs to a cluster to a degree that is specified by a membership grade [32]. The FCM method is initialized with a preliminary, usually incorrect, guess for the cluster centers, which are intended to correspond to the mean location of each cluster. Based on the initial estimates of the cluster centers, FCM assigns every data point a membership grade for each cluster. By iteratively updating the cluster centers and the membership grades for each data point, FCM moves the cluster centers to the “correct” location within a data set. This iteration is based on minimizing an objective function that represents the distance from any given data point to a cluster center weighted by that data point’s membership grade.

Since an unknown number of clusters are present in the data set, several potential cluster numbers were considered in order to determine the optimum number of clusters. The receiver operating characteristic, or ROC, curves for different cluster numbers were evaluated. Performance,

as measured by the ROCs, improved as the number of clusters was increased to  $n = 6$ ; however, adding additional clusters beyond 6 did not improve performance. Thus, six clusters were used in the pdfs describing both the mine and clutter hypotheses.

The contours that resulted from the automatic FCM clustering resembled a circle more than an ellipsoid, indicating that the FCM grouping method may have tended to underestimate correlation between the two decay rates in each cluster. Because of the absence of the correlation structure, the clustering results obtained with the FCM grouping method were quite different from those obtained using the brute-force grouping (see Fig. 2). This difference was also reflected in the ROC curves, as shown in Figure 3, which show the performance measured for each clustering scheme. The

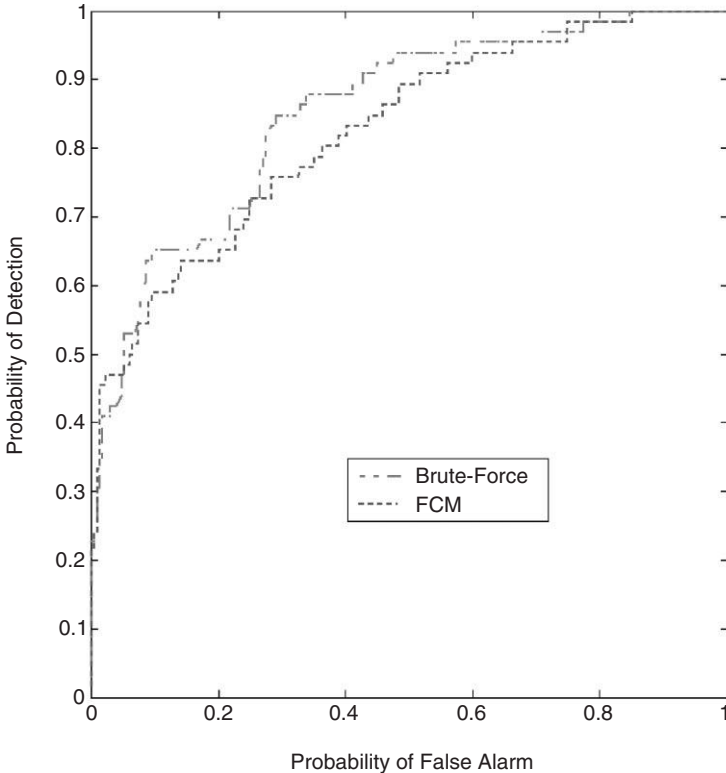


**Figure 3.** ROC curves for the brute force and FCM clustering methods. Probability of detection is plotted as a function of probability of false alarm, with the results for the brute force method shown with the dashed-dot curve and results for the FCM clustering algorithm shown with the dotted line.

statistical algorithm using the brute-force clustering slightly out-performed the algorithm using the FCM clustering. This indicates that the correlation structure that exists in the data can be utilized to improve performance. Since the FCM grouping resulted in slightly poorer performance than a brute-force grouping when the number of clusters was identical across each method, the brute-force grouping was used in all subsequent analyses.

To determine whether the decay rate processors, whose goal is discrimination, outperform the more traditional energy detectors, whose goal is solely detection, ROC curves were calculated for each of the three processors. In the calibration area, there are 21 mines, 20 clutter objects, and 59 blank squares. ROC curves are typically plotted as the probability of detection as a function of the probability of false alarm, and thus are plotted as such here. However, since  $H_0$  consists of the metallic clutter and blanks and  $H_1$  consists of mines only, the ROC curves are truly plotting probability of discrimination versus probability of false alarm.

The results shown in Figure 4 indicate that the performance of both the 1DR and 2DR processors are better than that of the energy processor, although the improvement in performance is not dramatic. This particular data collection site is focused on discrimination of low-metal mines from competing clutter, signals for which the PSS-12 was not optimally designed, thus the rather modest gains in performance shown in Figure 4 are not surprising. The 2DR processor does not provide substantially better performance than the 1DR processor, mainly improving the performance over the 1DR processor in the high probability of detection case. However, since the high probability of detection region of the ROC is where most human operators attempt to maintain their performance, especially for this application, it is possible that performance gains could be observed by using a 2DR processor if it is used to provide an audio signal to an operator. Although the performance of all three detectors converges at the point where the detection and false alarm probabilities are both 1, it is still possible to make relative performance comparisons above where the detection probability is approximately 90%. In this case, a 20% decrease in false alarm percentage corresponds to correctly rejecting approximately 4 clutter items.

#### 4. Auditory Display Design and Testing

The results presented in the previous section provide a theoretical argument indicating that alternative signal processing algorithms could reduce the number of false alarms due to metallic clutter that are obtained using simple signal strength metrics. It is important to determine whether this advantage can be translated into measurable changes in performance that can be achieved by an operator. In current operational landmine detection,

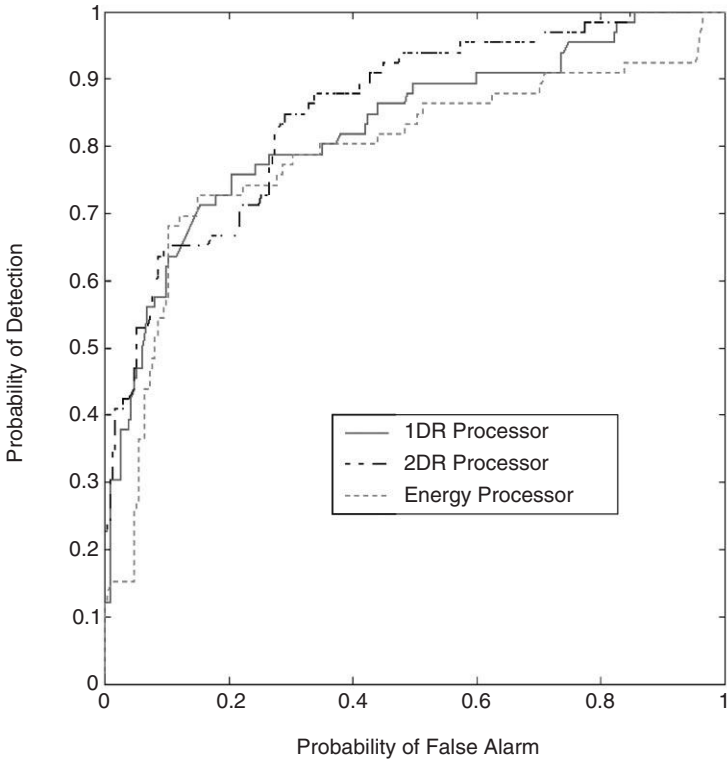


**Figure 4.** ROC curves for the 1DR, 2DR and energy processors. Probability of detection is plotted as a function of probability of false alarm, with the results for the energy processor shown with the dotted line, the 1DR processor with the solid line, and the 2DR processor with the dashed-dot line.

the ultimate decision of whether the target is a mine or clutter object relies on operators who sweep the field using hand-held EMI sensors, making decisions based on the processed audio signal that they hear. The audio signal is generated from a signal strength calculation, where the signal strength is proportional to the amount of metal that is detected and inversely proportional to the distance between the sensor and the object. A commonly used measure for the signal strength is the signal energy, and some parameter of the audio signal, usually frequency or amplitude, is modulated based on this signal strength.

The most commonly used method for generating an alarm sound for landmine detection systems is to change the frequency of the sound that is presented to the operator. The pitch or frequency of the audio signal is

determined by either the total energy or a single sample of the recorded signal in EMI systems. High-pitched sounds, corresponding to high-energy signals, indicate that high metallic content material is present in the environment. Based on the audio signal, it is possible for an operator to determine that an object is present when a high frequency alarm sound is heard. This audio coding scheme is based on the assumption that a signal from a mine has more energy than a signal from non-mine objects or the ground. However, some clutter objects are highly metallic and are, therefore, encoded as a high frequency sound, thus giving rise to the false alarm problem. Because operators want to be alerted to the presence of any object, be it a mine or not, any new audio alarm signal must still indicate that metal is present in the immediate environment. However the presence of metal alone does not indicate the presence of a mine. The hypothesis of this study is that coding additional information in the audio signal that reflects mine characteristics could potentially decrease the false alarm rate and improve discrimination.

This strategy could also potentially improve the discrimination of low-metal content mines that result in low energy signals in the detector, but have decay rates consistent with that of a mine. (It is important to note here that this assumes that all of the signals from metal objects are detectable by the sensor. Since the ROCs do not achieve detection probabilities of 1 until the false alarm probability is 1, this assumption is not true for this data set, for the reasons mentioned previously. However, we can still consider the discrimination performance improvements at detection probabilities slightly less than 1.) As described previously, the decay rates are an invariant feature of the signal recorded from time domain EMI sensors and are an inherent characteristic of mines. If the output of a decay rate processor drives one parameter of the alarm sound, such as loudness or repetition rate, while more traditional algorithms drive frequency content, discrimination performance may improve. To address this issue, two listening experiments were designed and conducted.

#### **4.1. Experiment 1—Familiarization with the Baseline System**

The goal of the first experiment was to familiarize listeners with the presentation methodology associated with the traditional signal processing performed by EMI systems. Effectively, this simulates the training process that soldiers undergo while training to use a standard metal detector. Based on the work of others [18,19], the basic alarm that was used consisted of an 11 component harmonic complex with an adjustable fundamental frequency, a duration of 500 ms, and an amplitude of 63 dB. The amplitude of the  $n$ th harmonic component was  $1/n$  that of the fundamental. The energy in the signal from the metal detector was mapped to one of a set of seven fundamental

frequencies: 210, 250, 280, 320, 440, 500, and 680 Hz. The energy distribution was discretized into seven equal-area sections and mapped to the seven fundamental frequencies. A 50 ms raised cosine window was used for the onset and offset of the signal. All stimuli were loudness balanced prior to presentation. Loudness balancing was necessary since sounds with different frequencies and the same amplitude have different perceived loudness levels, and it was important to remove overall loudness as a cue for the task in order to independently analyze the effects of each cue of interest in the subsequent experiment.

One male and four female subjects who were 25–28 years old participated in the experiments. Some subjects had participated in previous hearing experiments, but none had been tested on experiments similar to the ones performed in this study. Subjects performed the experiments while seated in a soundproof booth. They first performed the training experiments 5 times, and 60 trials were presented in each experiment. In each trial, a signal was selected randomly from the data set collected at the JUXOCO site. The energy of this signal was calculated and mapped through the previously defined nonlinear relationship to one of the seven fundamental frequencies. The harmonic signal corresponding to this frequency was then played through headphones in a one-interval forced-choice paradigm. (High quality headphones were not used specifically to simulate the types of headphones used by typical EMI system operators.) The probability that the signal was from a mine in each trial was 0.5. Although subjects were told that higher frequency sounds were more likely to represent mines, no criterion was set for the subjects, and feedback was not provided on a trial-to-trial basis. A reward/penalty scheme was utilized to aid subjects in setting a criterion that optimized their performance. After completion of each of the five training experiments, subjects were given a score as feedback. This mechanism reinforced the criterion that higher frequency signals were indicative of the presence of a landmine. Only five sets of sixty trials were used in this experiment to avoid over-training of the criteria, and to simulate the limited training usually provided to EMI system operators.

#### **4.2. Experiment 2—Investigation of the Stimulus Dimensions in which to Provide Additional Information**

The second set of experiments investigated whether additional information regarding the probability that a landmine was present could be conveyed to listeners through a separate stimulus dimension in order to improve discrimination performance. Two of the dimensions proposed for general alarm sounds that were suggested by Hellier *et al.* [19], loudness and pulse rate, were investigated. As preliminary steps, the decay rates were

extracted from the data measured by the PSS-12 system and the total energy of the signal was calculated. The decay rates were processed by the 1DR and 2DR algorithms and then used to drive either the loudness or the pulse rate of the stimulus. At the same time, the energy in the signal was used as in the training experiment to drive the fundamental frequency of the harmonic complex.

In these experiments, three approaches to information coding were tested:

- (1) Energy drives the fundamental frequency. The stimuli were the same as those that were used in the training experiments, and the results provided a baseline to which the discrimination performance achieved with the other information coding methodologies could be compared.
- (2) Energy drives the fundamental frequency and the output of one of the two DR processors drives loudness. The baseline loudness of each alarm sound was the same as that in the training experiment. The loudness was varied across 7 different levels, and the interval between each level was 3–4 dB, a difference that is discriminable for human subjects.
- (3) Energy drives the fundamental frequency and the output of one of the two DR processors drives the pulse rate. In this experiment, each pulse consisted of a harmonic complex that was identical to the basic alarm signal used in the training experiment with the exception that the duration of each complex was decreased to 200 ms. The duration of the pulse-train complex was approximately 2500 ms, and the number of pulses in the entire complex was one of 7 different levels. The parameters for this experiment are shown in Table 1.

In summary, there were five experiments performed to determine whether additional information could be coded in the audio signal and used by the

**Table 1. Parameters Associated with the Stimuli with Modulated Pulse Rates**

Level	Number of pulses	Interpulse interval (ms)	Duration (ms)
1	4	477.5	2232
2	5	302.0	2208
3	6	237.8	2389
4	8	117.7	2423
5	9	59.6	2536
6	10	50.0	2450
7	12	9.6	2504

subjects to improve their performance on the discrimination task. The baseline detection experiment was equivalent to the training experiment in which the energy in the signal drove the fundamental frequency of a harmonic complex. In the remaining four experiments, energy continued to drive the fundamental frequency. In addition, the 1DR or 2DR processor output drove either the loudness or the pulse rate of the audio signal that was presented to the subject. Each experiment was performed 5 times by each listener, with 60 trials presented in each experiment. Experiments were performed in random order. Subjects were informed that the baseline experiment was the same as the training system, and that the information being conveyed in the new dimension was provided as a measure of the confidence that a landmine was present. They were told that “louder” and “faster” for the loudness and pulse rate experiments, respectively, corresponded to “more mine like”.

The performance achieved by each subject in each one-interval forced choice experiment was calculated using a standard  $d'$  summary statistic. To calculate these  $d'$  values, an ROC for the binary detection problem is generated assuming that the decision statistic under  $H_1$  follows a Gaussian probability density function with mean  $\mu_1$  and variance  $\sigma^2$  and that the decision statistic under  $H_0$  follows a Gaussian probability density function with mean  $\mu_0$  and variance  $\sigma^2$ . Using the results of each experiment, a probability of detection and probability of false alarm were calculated. Then, the ROC for the binary detection problem with a difference in the means,  $\mu_1 - \mu_0$ , and variance  $\sigma^2$  was posed, and a mean difference and variance were found such that the assumed ROC intersected the experimental probabilities. The  $d'$  was then calculated using  $(\mu_1 - \mu_0 / \sigma)$ .

The  $d'$  values across the five repeated runs of the experiment were averaged to obtain a final score for each experimental condition. The average  $d'$  value for each experiment is plotted as a function of subject number in Figure 5. Performance for each experiment is shown with the same symbol for each subject and lines connect the symbols in order to assist in the interpretation of the results. Several conclusions can be drawn from the experimental results shown in Figure 5. Generally, using the 1DR or 2DR processor output to drive any parameter of the audio signal in addition to having the energy drive the fundamental frequency improves the discrimination performance. The theoretical results provided in the previous section predicted such a trend. We may therefore hypothesize that utilizing energy and decay rate processors to generate an audio signal may improve discrimination performance because additional statistical information from the signal is used.

Of the two acoustic parameters employed, modulating the pulse rate appears to improve discrimination performance more than does the modulation of loudness. In an acoustic sense, changes in pulse rate alter the

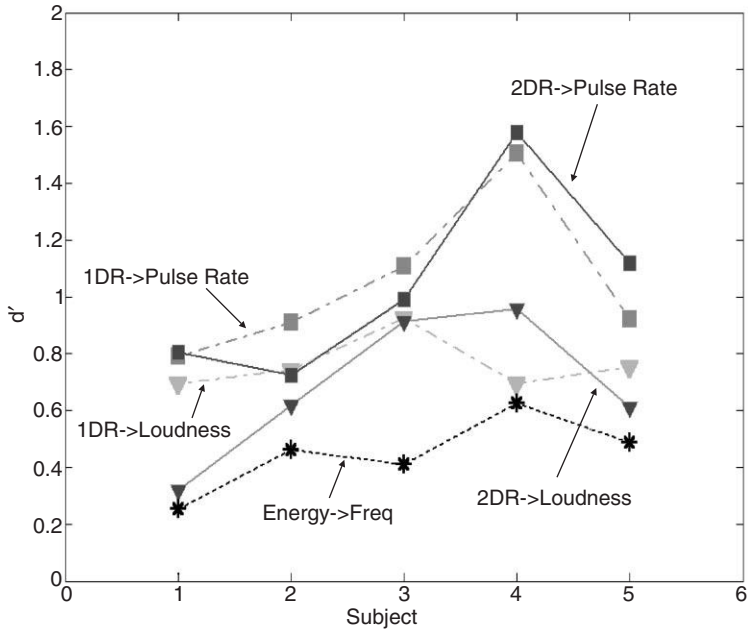


**Figure 5.** Performance on the five experiments is measured as  $d'$  and is plotted for each of the four subjects. Performance for each experiment is shown with the same symbol as a function of subject number and are connected by lines to aid interpretation.

character of the stimulus and may be more discriminable than changes in loudness that only alter the quality of the signal. The results shown in Figure 5 also indicate that training may be an issue since the results obtained by subject 4 are substantially better than the results obtained by any of the other subjects. It is possible that subject 4 understood the task and/or the instructions better than the other subjects, and thus performed better, and that additional training or more detailed explanations and instructions could help improve the scores of the other subjects. Future work will investigate the effect of training more carefully. However, in this study we were specifically interested in whether untrained subjects (like untrained soldiers) could obtain any benefit from the additional information provided by the decay rate processor. The results in Figure 5 clearly indicate that subjects can use additional information when it is provided.

The left panel of Figure 6 illustrates the ROCs that would be obtained using the mean  $d'$  across subjects for each experiment and assuming that the underlying perceptual variables (which are unknown) follow a Gaussian distribution. Again, the results indicate that the addition of any information

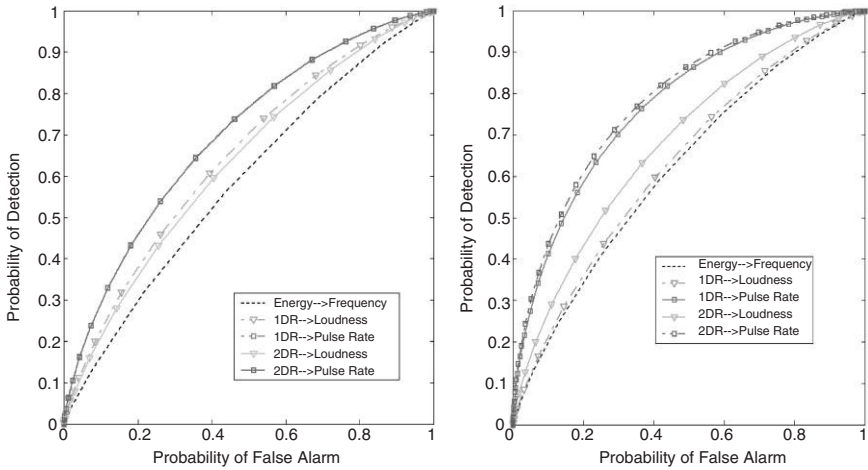


Figure 6. ROC curves generated using the average  $d'$  across the five subjects (left panel) and the  $d'$  values from the best subject (right panel).

beyond simple energy will improve average discrimination performance over baseline detection performance. The right panel of Figure 6 illustrates the ROCs that would be obtained using the  $d'$  measured for the best subject's performance and the same Gaussian assumption. These results can be compared to those shown in Figure 4, which provide the theoretical performance bounds for this experiment. These results provide an upper bound since the automated algorithms were trained and tested on the same data set. Although the best subject does not achieve the bound, these results were obtained without training. It is possible that with training, subjects could approach the performance bound.

### 5. Discussion

In applications such as humanitarian demining, EMI sensors are often used to locate every metallic object in the area to be cleared. Some of the metallic anomalies that are detected will be landmines, while others will be clutter. We, along with others, have shown that advanced signal processing algorithms can be used to discriminate landmines from clutter using EMI data. In these algorithms, signals from "clutter" often result in a low level output from the algorithm while signals from landmines result in a high level output. In military and humanitarian demining scenarios, the operator should be provided with both the knowledge that a metallic object is present, even when that object is not a landmine, and an indication of whether a particular object is a landmine or a clutter object.

The results of this study indicate that by using the energy in the measured signal to drive the frequency of an audio alarm signal and using the output of a more advanced algorithm to drive other parameters of the audio signal, an operator can be provided with both pieces of information in an interpretable format. Such an alarm system design approach in which additional information beyond metal content is extracted and provided to the user has not been tested previously in this application area. Using this approach, untrained subjects improve their ability to discriminate mines from clutter, for real landmine data collected in the field. Our results are consistent with those in the literature for other applications [18,19] in that they indicate that changing the pulse rate of an alarm signal provides better perception of urgency than changes in loudness, and thus better discrimination of signals of interest from those that are not of interest. However, the information that metal has been detected persists in the presentation that we have proposed. Our results also indicate fairly dramatic inter-subject differences in overall level of discrimination, suggesting that training may be an issue.

## Acknowledgments

The authors would like to thank Chandra Throckmorton and David Ferguson for their assistance with the experimental protocol, and the subjects for their time and effort. This research was sponsored by the Army Research Office under grant DAAG55-98-1-0416.

## References

1. Strada, G., 1996, The horror of landmines: Scientific American.
2. Riggs, L.S., Mooney, J.E., and Lawrence, D.E., 2001, Identification of metallic mine-like objects using low frequency magnetic fields: *IEEE Trans. Geosci. Remote Sens.*, v. 39, no. 1, p. 56–66.
3. Sower, G.D. and Cave, S.P., 1995, Detection and identification of mines from natural magnetic and electromagnetic resonances: *Proc. of SPIE, Orlando, FL*.
4. Trang, A.H., Czipott, P.V., and Waldron, D.A., 1997, Characterization of small metallic objects and non-metallic anti-personnel mines: *Proc. of SPIE, Orlando, FL*.
5. Das, Y., McFee, J.E., Toews, J., and Stuart, G.C., 1990, Analysis of an electromagnetic induction detector for real-time location of buried objects: *IEEE Trans. Geosci. Remote Sens.*, v. 28, p. 278–288.
6. Miller, J.T., Bell, T.H., Soukup, J., and Keiswetter, D., 2001, Simple phenomenological models for wideband frequency-domain electromagnetic induction: *IEEE Trans. Geosci. Remote Sens.*, v. 39, no. 6, p. 1294–1298.
7. Tantum, S.L. and Collins, L.M., 2001, A comparison of algorithms for subsurface object detection and identification using time domain electromagnetic induction data: *IEEE Trans. Geosci. Remote Sens.*, v. 39, no. 6, p. 1299–1306.
8. Gao, P., Collins, L., Garber, P., Geng, N., and Carin, L., 2000, Classification of landmine-like metal targets using wideband electromagnetic induction: *IEEE Trans. Geosci. Remote Sens.*, v. 38, no. 3, p. 1352–1361.

9. Gao, P. and Collins, L., 1999, A comparison of optimal and sub-optimal processors for classification of buried metal objects: *IEEE Signal Processing Letters*, v. 6, no. 8, p. 216–218.
10. Collins, L., Gao, P., and Carin, L., 1999, An improved Bayesian decision theoretic approach for land mine detection: *IEEE Trans. Geosci. Remote Sens.*, v. 37, no. 2, p. 811–819.
11. Gao, P. and Collins, L., 2000, A 2-dimensional generalized likelihood ratio test for landmine detection: *Signal Processing*, v. 80, p. 1669–1686.
12. Carin, L., Yu, H., Dalichaouch, Y., and Baum, C., 2001, On the wideband EMI response of a rotationally symmetric permeable and conducting target: *IEEE Trans. Geosci. Remote Sens.*, v. 39, no. 6, p. 1206–1113.
13. Gelenbe, E. and Kocak, T., 2000, Area-based results for mine detection: *IEEE Trans. Geosci. Remote Sens.*, v. 38, p. 12–24.
14. Won, I.J., Keiswetter, D.A., and Bell, T.H., 2001, Electromagnetic induction spectroscopy for clearing landmines: *IEEE Trans. Geosci. Remote Sens.*, v. 39, no. 4, p. 703–709.
15. Nelson, C.V., Cooperman, C.B., Schneider, W., Wenstrand, D.S., and Smith, D.G., 2001, Wide bandwidth time-domain electromagnetic sensor for metal target classification: *IEEE Trans. Geosci. Remote Sens.*, v. 39, no. 6, p. 1129–1138.
16. Staszewski, J. and Davison, A., 2000, Mine detection training based on expert skill, in Dubey A.C., Harvey J.F., Broach J.T., and Dugan R.E. (eds.), *Detection and remediation technologies for mines and mine-like targets V: Proc. of Soc. of Photo-Optical Instrumentation Engineers 14th Annual Meeting*, SPIE v. 4038, p. 90–101.
17. Staszewski, J., 2001, Expert analysis and training: Using cognitive engineering to develop mine detection skill: *Demining Technology Information Forum J.*, 1, [http://www.maic.jmu.edu/dtif/toc\\_dtif.html](http://www.maic.jmu.edu/dtif/toc_dtif.html).
18. Patterson, R.D., 1982, *Guideline for auditory warning systems on civil aircraft: Civil aviation Authority Paper 82017*.
19. Hellier, E.J., Edworthy, J., and Dennis, I., 1993, Improving auditory warning design: Quantifying and predicting the effects of different warning parameters on perceived urgency: *Human Factors*, v. 35, p. 693–706.
20. Ferguson, G., Vause, N., Mermagen, T., and Letowski, T., 2000, Auditory signals for enhanced operator performance with hand-held mine detectors, in Dubey A.C., Harvey J.F., Broach J.T., and Dugan R.E. (eds.), *Detection and remediation technologies for mines and mine-like targets V: Proc. of Soc. of Photo-Optical Instrumentation Engineers 14th Annual Meeting*, SPIE v. 4038, p. 130–135.
21. Baum, C.E., 1993, Low-frequency near field magnetic scattering from highly, but not perfectly, conducting bodies: *Phillips Laboratory Interaction Note 499*.
22. Das, Y., McFee, J.E., and Cherry, R.H., 1984, Time-domain response of a sphere in the field of a coil: Theory and experiment: *IEEE Trans. Geosci. Remote Sens.*, v. GE-22, p. 360–367.
23. Das, Y. and McFee, J.E., 1990, A simple analysis of the electromagnetic response of buried conducting objects: *IEEE Trans. Geosci. Remote Sens.*, v. GE-28, p. 278–288.
24. Geng, N., Baum, C.E., and Carin, L., On the low-frequency natural response of conducting and permeable targets: *IEEE Trans. Geosci. Remote Sens.*
25. Steedly, W.M. and Moses, R.L., 1993, The Cramer–Rao lower bound for pole and amplitude coefficient estimates of damped exponential signals in noise: *IEEE Trans. Signal Processing*, v. 41, p. 1305–1318.
26. Tantom, S. and Collins, L., 2001, Robust statistical signal processing for subsurface target detection and identification: *National Radio Science Meeting*, Boulder, CO.
27. Riggs, L., 1999, Operating characteristics of the AN-PSS12: *Technical Report*, JUXOCO, Ft. Belvoir, VA.
28. JUXOCO, 1998, Hand held metallic mine detector performance baselining collection plan: *JUXOCO*, Ft. Belvoir, VA.

29. Collins, L., Gao, P., Moulton, J., Makowsky, L., Reidy, D., and Weaver, R., A statistical approach to landmine detection using broadband electromagnetic induction data: submitted to *Trans. Geosci. Remote Sens.*
30. Tantum, S. and Collins, L., Improved decay rate estimation via a parameter transformation: submitted to *IEEE Signal Processing Letters*.
31. Van Trees, H.L., 1968, *Detection, estimation, and modulation theory, Pt. I.*, John Wiley and Sons, Inc., New York, NY.
32. Dunn, J.C., 1974, A Fuzzy relative of the ISODATA process and its use in detecting compact, well separated clusters: *J. Cybern.*, v. 3, p. 32–57.